Hindawi Publishing Corporation
Laser Chemistry
Volume 2011, Article ID 140976, 27 pages
doi:10.1155/2011/140976

Research Article

Oxide Thin Film Heterostructures on Large Area, with Flexible Doping, Low Dislocation Density, and Abrupt Interfaces: Grown by Pulsed Laser Deposition

Michael Lorenz, Holger Hochmuth, Christoph Grüner, Helena Hilmer, Alexander Lajn, Daniel Spemann, Matthias Brandt, Jan Zippel, Rüdiger Schmidt-Grund, Holger von Wenckstern, and Marius Grundmann

Institut für Experimentelle Physik II, Fakultät für Physik und Geowissenschaften, Universität Leipzig, Linnéstraße 5, 04103 Leipzig, Germany

Correspondence should be addressed to Michael Lorenz, mlorenz@physik.uni-leipzig.de

Received 13 August 2010; Accepted 21 September 2010

Academic Editor: Alciviadis-Constantinos Cefalas

Advanced Pulsed Laser Deposition (PLD) processes allow the growth of oxide thin film heterostructures on large area substrates up to 4-inch diameter, with flexible and controlled doping, low dislocation density, and abrupt interfaces. These PLD processes are discussed and their capabilities demonstrated using selected results of structural, electrical, and optical characterization of superconducting ($YBa_2Cu_3O_{7-\delta}$), semiconducting (ZnO-based), and ferroelectric ($BaTiO_3$-based) and dielectric (wide-gap oxide) thin films and multilayers. Regarding the homogeneity on large area of structure and electrical properties, flexibility of doping, and state-of-the-art electronic and optical performance, the comparably simple PLD processes are now advantageous or at least fully competitive to Metal Organic Chemical Vapor Deposition or Molecular Beam Epitaxy. In particular, the high flexibility connected with high film quality makes PLD a more and more widespread growth technique in oxide research.

1. Introduction

Pulsed Laser Deposition (PLD) is a relatively new exploratory growth technique especially suitable for oxide thin films and heterostructures [1, 2]. In contrast to other, "older" physical deposition techniques as, for example, thermal evaporation and molecular beam epitaxy (MBE), or cathode sputtering, the development of the "younger" PLD technique was considerably speeded up by the first successful epitaxy of high-T_c superconducting thin films by Venkatesan after 1986 [3, 4].

The principle of PLD is the use of a small single source target with diameter of about one inch, which may be a single- or a multicomponent compound material [5]. An ns-pulse high-power laser with wavelength in the UV ablates material from the target and excites it into a plasma state. This plasma propagates with particle energies up to about 100 eV perpendicularly to the target surface and condenses as thin film on the substrate. Well-established advantages of PLD are the unique flexibility concerning the deposited film material, the high growth rate, and a high structural quality of the films. Due to the spatial decoupling of the laser as main plasma energy source and the growth chamber, the PLD parameters such as the background gas partial pressure and the growth temperature can be varied in a uniquely wide range. Furthermore, often congruent ablation and deposition of multielement compounds are found, resulting in a stoichiometric transfer of the compound target material into the thin film [5]. However, several drawbacks are generally thought to limit the application of PLD, as for example, the small substrate area of usually not more than one cm^2, sometimes rough surfaces and interfaces,

and also particulates and droplets on the films. Sometimes, deviations from the stoichiometric transfer may influence a controlled doping and alloying. Furthermore, because of the highly nonlinear, pulsed nature of the deposition process, very smooth surfaces and interfaces are not always easy to obtain with PLD [6]. In heteroepitaxial growth of films on substrates of different compounds, the misfit and differences in thermal expansion coefficients induce usually high densities of dislocation lines [7].

Therefore, the aim of this paper is to show how we are able to practically overcome some of these above-mentioned limitations in PLD of oxides. First we will demonstrate the possibilities of PLD to grow complex multielement compounds, as for example, the high-T_c superconductor $YBa_2Cu_3O_{7-\delta}$, doped ZnO semiconductor layers, or all-oxide optical multilayers, so called Bragg reflectors, with high lateral homogeneity on large area sapphire or silicon substrates with 2-inch, 3-inch, or even 4-inch diameter. A particular challenge concerning the high-T_c $YBa_2Cu_3O_{7-\delta}$ films was to grow them not only on one substrate side as it is the usual case, but on both front and back sides of a 3-inch or 4-inch diameter sapphire wafer. For the films deposited on the two wafer sides, similar high electrical performance and homogeneity were required.

Next, we will discuss the possibilities to grow doped and alloyed materials. This concern is in particular the II-VI semiconductor ZnO [6, 8] which was doped with donors, potential acceptor elements, and 3d elements to induce a "diluted" ferromagnetism. The ferroelectric thin film material $BaTiO_3$ was doped with several transition metal oxides to reduce dielectric loss and to tune the temperature dependence of the permittivity. Here, also the occurrence of trace impurities in the films will be discussed, which may act as unintentional electrically or magnetically active dopant.

The third main section deals with growth of thin films with reduced structural defects to enhance electrical properties as, for example, the free carrier mobility in the oxide semiconductor ZnO. Here, we used a multistep-PLD process with low-temperature intermediate layers to reduce the strain and by this the dislocation density in heteroepitaxial ZnO thin films. Much lower defect densities are obtained in homoepitaxial ZnO growth on ZnO single crystals, and high Hall mobilities up to 800 cm^2/Vs below 100 K were measured.

Finally, recent results on the growth of very abrupt MgZnO-ZnO quantum well structures with well widths in the range 1–7 nm are shown. These structures grown by a specially optimized PLD process with reduced laser energy density show strong quantum-confined Stark effect which appears as a measure of the abruptness of the embedded quantum well nanolayers. A new PLD setup with an in situ high-pressure RHEED allows the monolayer growth control in $SrTO_3$-$BaTiO_3$ multilayers through the observation of RHEED monolayer oscillations.

The presented results give an overview on the state of the art capability of PLD for growth of advanced oxide thin film structures for basic and applied investigations up to the level of fully functional demonstrator devices.

2. Basics and Experimental

In this section selected aspects of modelling of the PLD process (Section 2.1) are discussed. Our modular PLD deposition chambers with large-area heaters up to 4-inch diameter, suitable for double-sided deposition, are shown in Section 2.2. Optical emission spectra of the laser plumes of the typically deposited materials are presented in Section 2.3.

2.1. Modelling of PLD Process. After 1987, the number of publications on basics and applications of PLD increased exponentially, and more and more material systems were deposited successfully with PLD [1, 2, 5–7]. Beside the bulk of published papers (see [6]), also several PhD theses give more details about basic understanding and application of PLD to selected materials as, for example,

(a) ferroelectrics, for example, $BaTiO_3$ and $PbZr_xTi_{1-x}O_3$, also $BaTiO_3/SrTiO_3$ multilayers, by Curran [12], Klarmann [13], Köbernik [14], Maier [15], Mertin [16], Petraru [17], Siegert [18],

(b) dielectric oxides as, for example, Y_2O_3, $SrTiO_3$, MgO, Sc_2O_3, $Y_3Al_5O_{12}$, YSZ, by Bar [19], Goldfuß [20], Hobein [21], Hühne [22], Keiper [23], Kuzminykh [24],

(c) high-T_c superconducting oxides, by Ferchland [25], Maier [15], Schey [26], Wörz [27],

(d) nitrides as BN, AlN, by Hohage [28], Six [29],

(e) carbon nanotubes by Gorbunoff [30], nonoxide ternary semiconductors by Roussak [31], Mo/Si multilayers by Braun [32], Nd-Fe-B layers by Hannemann [33], diamond-like carbon by Thärigen [34] and Mercado [35], Ni-C multilayers by Sewing [36],

(f) ZnO, by Jin [37], Nobis [38], Rahm [39], Czekalla [40], and Brandt [41].

The fundamental physical processes of PLD and results of plasma diagnostics are discussed in [1, 2, 5, 6] and in addition in [16, 19, 29, 30, 42]. Up to now, a comprehensive model of the different processes during PLD with remarkable impact on the experiment does not exist. In the following we mention briefly some results which are important for the description of the innovative PLD processes.

Usually, the PLD process will be divided into the following three spatially separated sections, as shown in Figure 1, namely, (1) laser interaction with the source target, (2) plasma expansion, and (3) film growth on the substrate [16, 19, 43]. The ablation of atoms, ions, and clusters can be considered in many cases as a classical thermal evaporation process [29]. In addition, photoablation, that is, electronic sputtering, may participate as nonthermal ablation process [37]. In case of weakly absorbing target materials as, for example, dielectrics, the ablation will be due to laser-induced decomposition (dielectric breakdown) [19]. The laser absorption of materials with energy band gap above the laser photon energy (as, e.g., MgO, Al_2O_3) can be increased by the use of sintered targets with many grain boundaries and defects [29].

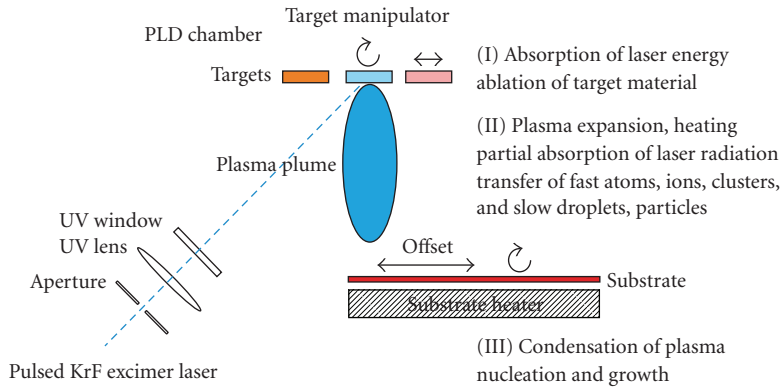

Figure 1: Scheme of a typical PLD setup for large-area "offset" film growth with the main functional components. The three fundamental process steps during (I) target ablation, (II) plasma expansion, and (III) film nucleation and growth are shortly described at the right. The "offset" distance has to be adjusted for laterally homogeneous films growth, as explained in Section 3 on large-area PLD.

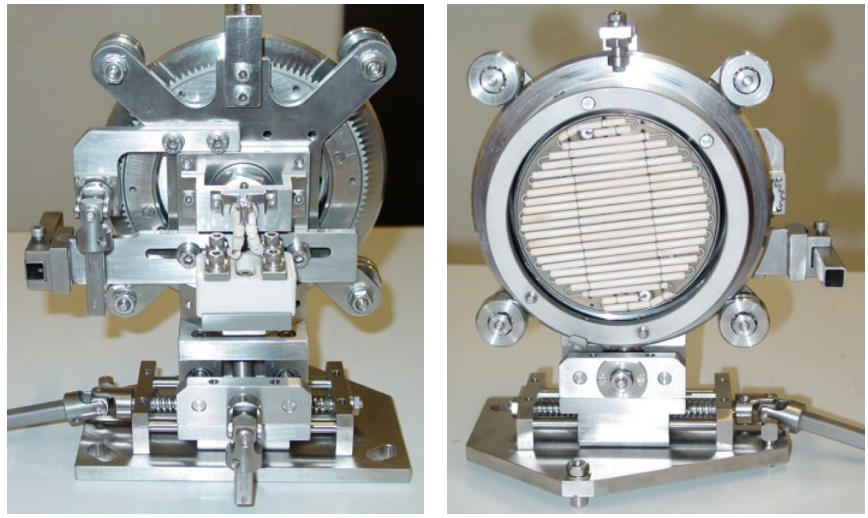

(a) (b)

Figure 2: Back side (a) and front side (b) of the modular PLD substrate heater (design and construction D. Natusch, Leipzig) for 3-inch diameter substrates, suitable for homogeneous double-sided deposition of oxide thin films. The active heater element is KANTHAL wire, embedded in alumina ceramic tubes. To reduce the temperature gradient to the substrate edge, an additional front side heater element is applied (not included in the photos).

Concerning the energy balance of incoming laser pulse energy (100%), only about 4% will be used to ablate material from the target, as deduced from reflectivity measurements and a heat conduction model for excimer laser ablation of $BaTiO_3$ for 2 J/cm^2 laser pulse energy [16]. About 64% of incoming laser energy will be absorbed in the plasma above the target surface, another 4% will be reflected from the target surface, and 28% go by heat conduction into deeper regions of the target. As undesired processes, the laser-target interaction includes the emergence of particulates and droplets by exfoliation and hydrodynamic sputtering, respectively. However, several techniques were developed to reduce the droplet density at the deposited films, as for example, perpendicular arrangements of target and substrate surface, velocity filters, or two-laser beam configurations [1, 2].

The adiabatic plasma expansion can be described by a hydrodynamic model with the Navier-Stokes equation [16]. The spatial plasma expansion is determined by a certain angular distribution of the form $(a\cos\Theta + b\cos^n\Theta)$, with Θ being the angle to the target normal, and the exponent n is in between 3 and 12, in maximum also up to 30, in dependence on the laser parameters and focus size, as pointed out by Saenger in [1]. In addition, the background gas pressure influences the angular plasma expansion considerably by scattering processes. Tillack has combined numerical predictions and experimental results to assess the competing effects of ionization and supersaturation [42]. For example, the time-dependencies of laser energy density, of target surface temperature, and of plasma velocity profiles were deduced from a one-dimensional model of the laser plasma. This model includes laser absorption, the thermal

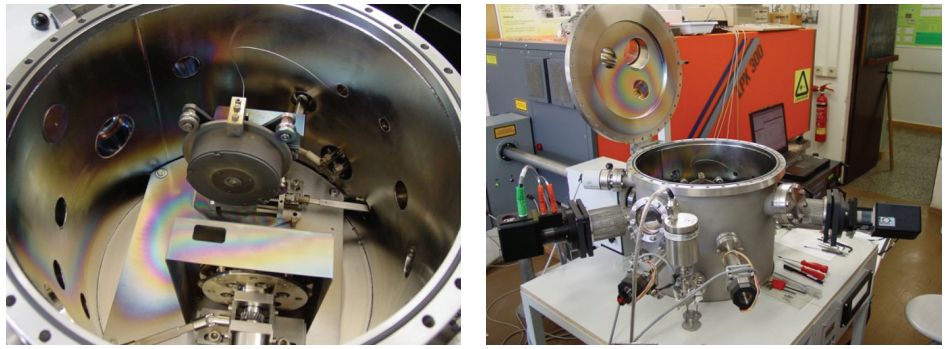

(a) (b)

Figure 3: Inner (a) and outer (b) view of our modular medium-size PLD chamber with in-situ-spectroscopic ellipsometer Woollam M 2000 and modular 3-inch diameter heater (see Figure 2) and target manipulator. The laser entrance window is top left under 45° incidence on the target. Additional shields (not included here) may reduce the unavoidable coating of the SUPRASIL plan parallel plate used as laser entrance. The position of the whole substrate heater (left photo) can be adjusted parallel to the substrate surface in order to change the offset distance for the large-area "offset" PLD (see Figure 1).

Figure 4: Photograph of the PLD plasma plume of ZnO in 0.16 mbar O_2 background gas in the PLD chamber shown in Figure 3. The light for the OES spectra was collected from the bright emission plume at 20 mm from the target surface at the left side. Photo was taken by C. Hanisch, University of Leipzig.

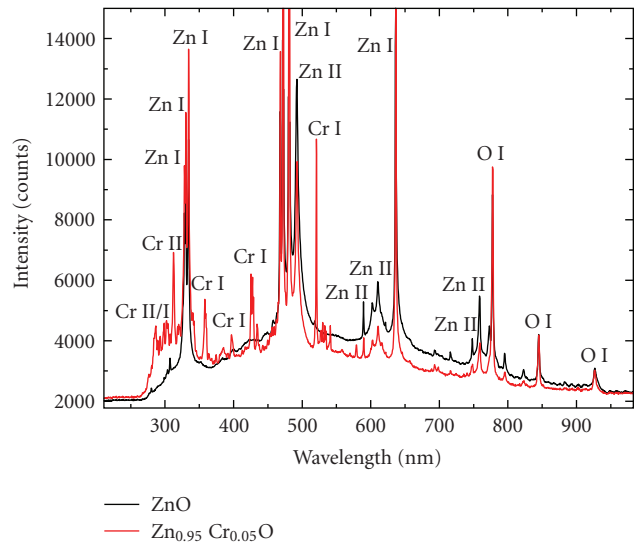

Figure 5: OES spectra taken from PLD plumes of pure ZnO (black curve) and of ZnCrO with 5% Cr (red curve), both in 0.1 mbar O_2. The emission intensities of ZnO and the fluorescence background in the Cr-doped ZnO are remarkably reduced in relation to the pure ZnO emission.

surface behavior, mass transfer, the plasma ionization (Saha equation) and recombination, and the hydrodynamics of the gas phase, the heat transport, and the cluster growth [42]. We conclude that all the above-mentioned results on plasma diagnostics in PLD experiments are valid only for very certain experimental conditions [29] and generalizations are difficult.

The growth mode and the film properties at PLD are mainly determined by the substrate temperature and the supersaturation $\Delta m = kT \ln(R/R_e)$ [37], R being the real and R_e the equilibrium deposition rate at temperature T. Due to the extremely high growth rate, the supersaturation of plasma flow may be up to 10^5 J/mol, which often stimulates a 2-dimensional growth with monolayer steps [37]. In heteroepitaxy, the growth will be lattice matched (pseudomorphic), domain-matched, or relaxed in dependence on the lattice mismatch, the film thickness, and the materials combination. In domain-matched epitaxy with in-plane lattice mismatch above 7%, for the ZnO(0001) growth on c-plane sapphire, there is a fit of 5 to 6 ZnO-$(2\bar{1}\bar{1}0)$ lattice planes to 6 or 7 α-$Al_2O_3(30\bar{3}0)$ planes, respectively [37, 45].

Up to now, the experimental variation of the PLD parameters is the only feasible method for the optimisation of the experimental PLD growth because, as explained above, a comprehensive modelling of the strongly nonlinear processes in PLD including ablation of target material, plasma emergence, plasma expansion, condensation, and film growth is not possible so far. However, specific parts of

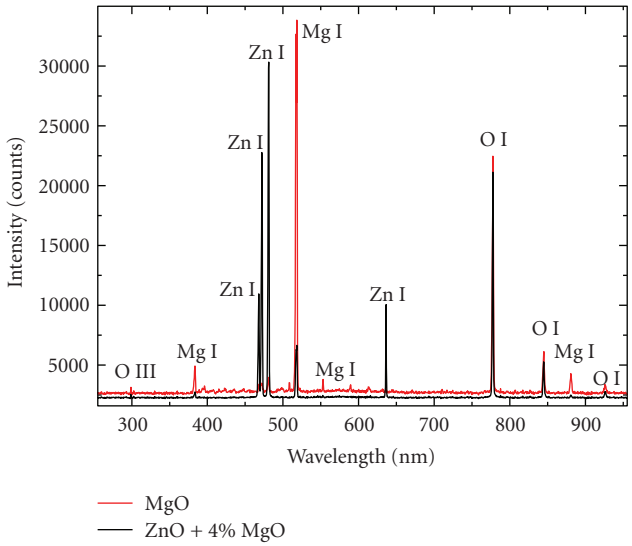

Figure 6: OES spectra taken from PLD plumes of pure MgO (red spectrum) and of ZnO with 4% MgO (black spectrum) in 0.1 mbar O_2.

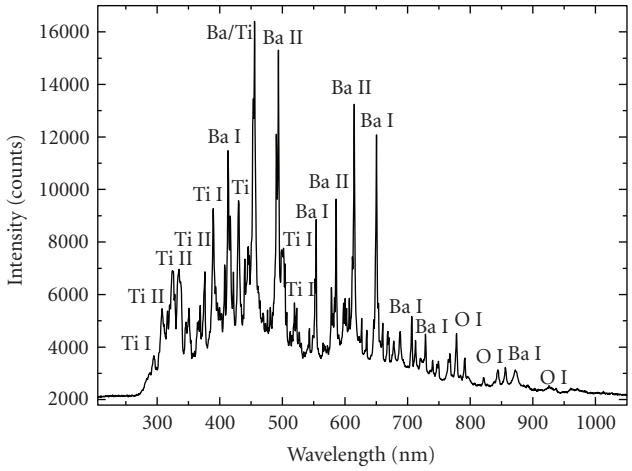

Figure 7: OES spectrum taken from PLD plume of $BaTiO_3$ in 0.1 mbar O_2. We have identified about 21 Ti and 19 Ba lines.

the PLD process can be treated by present models in good correlation to the experimental behavior.

2.2. Modular PLD Chambers for Large-Area Deposition. From the year 1990, the Leipzig PLD group has developed, designed, built, and optimized their PLD chambers in-house according to the requirements of the running projects [43]. Up to 2003, 3-inch and 4-inch diameter, double-sided high-T_c superconducting $YBa_2Cu_3O_{7-\delta}$ thin films for microwave applications were developed together with Robert BOSCH GmbH Stuttgart and other partners. From 2000, other oxide materials as the ferroelectric $BaTiO_3$ and the semiconducting ZnO [6] replaced the $YBa_2Cu_3O_{7-\delta}$ as main material under investigation.

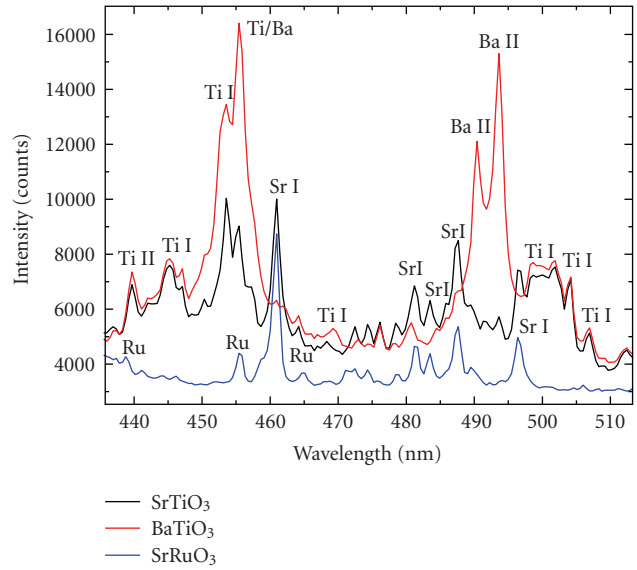

Figure 8: OES spectra taken from PLD plumes of $SrTiO_3$, $BaTiO_3$, and $SrRuO_3$ in 0.1 mbar O_2, in the wavelength range from 435 to 515 nm. For ruthenium only 2 lines could be clearly identified, while for Sr, Ti, and Ba about 20 lines were found from 250 to 1,000 nm wavelength.

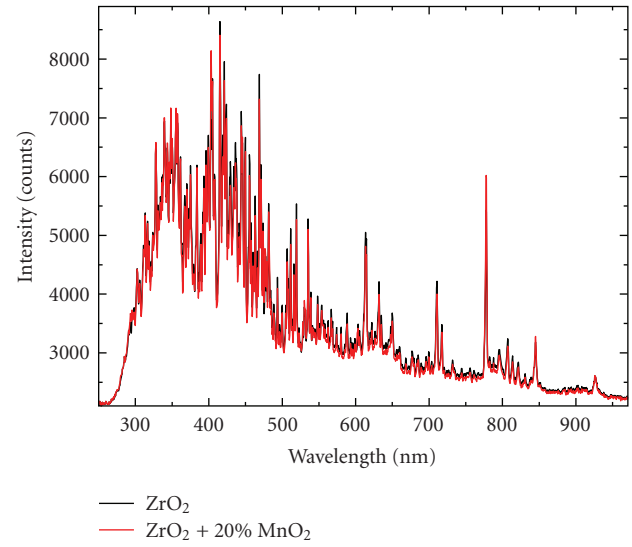

Figure 9: OES spectra taken from PLD plumes of pure ZrO_2 and of ZrO_2 with 20% MnO_2 in 0.1 mbar O_2. Only one additional peak from Mn I was found at 476.61 nm. In contradiction, Mn-doped ZnO shows 10 peaks from Mn. Zirconium and hafnium show together 1497 lines in the OES data base. A strong fluorescence background is visible here.

Within the last 20 years, 8 complete PLD systems including modular large-area substrate heaters with maximum substrate diameter of 3-inch or 4-inch (see Figures 2 and 3) and target manipulators were developed and built.

In particular, the large-area substrate heater as shown in Figure 2 is the result of a series of prototype heaters with different designs of the heater element and the substrate

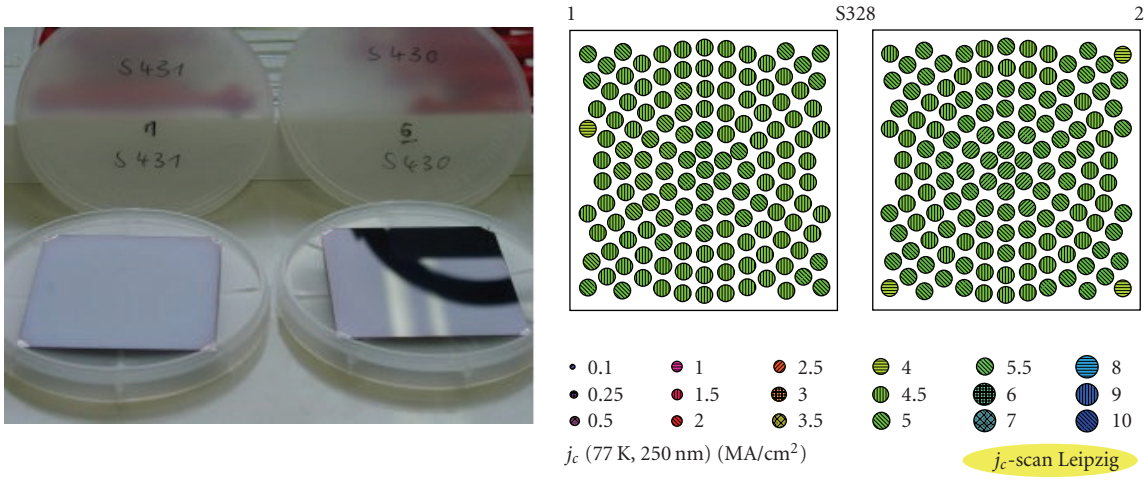

Figure 10: (a) Photograph of two double-sided YBCO wafers on $71 \times 75\,\text{mm}^2$ r-plane sapphire substrates with CeO_2 buffer layers. Obvious is the mirror-like, homogeneous appearance of the YBCO films. (b) Mapping of the critical current density (77 K) of such a $71 \times 75\,\text{mm}^2$ YBCO wafer with two YBCO films at both wafer sides, demonstrating the very good homogeneity of j_c using the "j_c-scan Leipzig." As much as 15 consecutively deposited $71 \times 75\,\text{mm}^2$ YBCO wafers showed such excellent j_c-homogeneity, indicating a high reproducibility of the "space qualified" large-area PLD process [9–11].

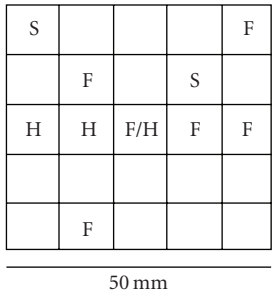

Figure 11: Schematic overview of the detailed sample positions for the presented measurements (S: SEM thickness, H: Hall effect, F: field effect mobility and transconductance) on the $50 \times 50\,\text{mm}^2$ a-plane sapphire substrate.

rotation. The current design allows a homogeneous and reproducible radiative substrate heating with low trace element contamination and therefore determines the state of the art of heater development [46]; see also [6] which shows further details of our PLD development. For higher growth temperatures above 800°C, much more expensive laser or SiC heaters are necessary [47]. In addition to the hardware part, a PLD process control software was written in Pascal (Delphi 2007 for Win32) which runs on normal personal computers. This PLD software controls all external devices of the PLD system including the Coherent (Lambda Physik) LPX 305 KrF excimer lasers and was adapted recently to Windows XP.

Table 1 summarizes typical conditions of our PLD processes for thin films and nanostructures. For more details of the the high-pressure "nanowire" PLD process, see [6, 48]. Typical for our low-pressure film growth processes is the target to substrate distance around 100 mm. In combination with the offset distance of projected center of target

Table 1: Typical parameters for PLD growth of thin film-like structures (at low partial gas pressure) and of nanowires (at high pressure). The offset is the distance from projected center of the target to center of the substrate, to ensure the homogenous large-area deposition with continuous substrate rotation.

Parameter	Low-pressure "film" PLD	High-pressure "nanowire" PLD
Grown materials	Highly flexible for oxides, for example, YBCO, $BaTiO_3$, ZnO, $ZnFe_2O_4$,...	ZnO, ZnMgO
Used substrates	Single-crystalline oxides, for example, Al_2O_3 ZnO, $SrTiO_3$..., or SiO_2 glass	Sapphire Al_2O_3 with gold colloides for nucleation.
Dopants	Highly flexible to the host oxide	P, Li, Al, Mn, Co
Background gas	O_2, N_2, N_2O	Ar
Background pressure	10^{-5} to 3 mbar	50 to 200 mbar
Gas flow rate	N/A	50 sccm @ 100 mbar
Growth temperature	20 to 770 °C	420–940 °C
Laser fluence	1 to 5 J/cm^2	2 J/cm^2
Target-substr.distance	100 mm	5 to 40 mm
Offset distance	0 to 35 mm	N/A

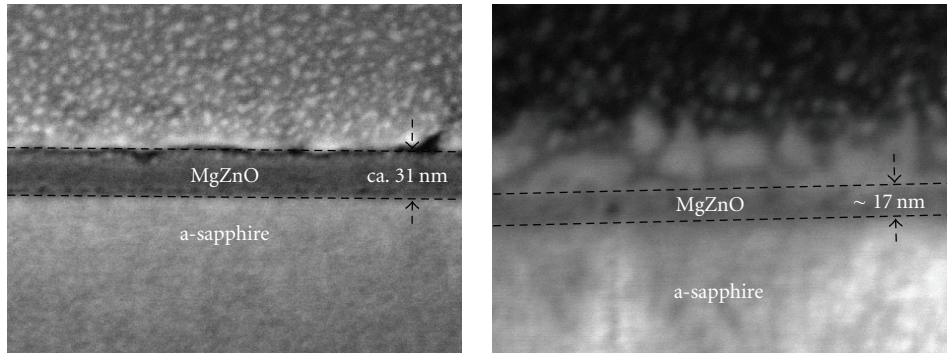

Figure 12: Cross-sectional microscopic image of MgZnO thin film in vicinity of the substrate center (a) and at the substrate edge (b). For the detailed positions of these samples within the 50 × 50 mm^2 wafer, see Figure 11.

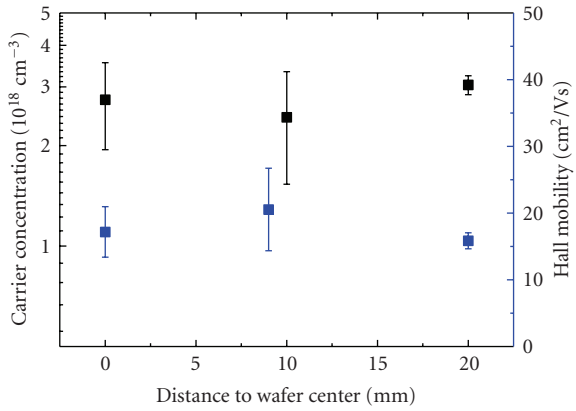

Figure 13: Variation of the free charge carrier density and the mobility determined by Hall-effect measurements over the substrate, as shown in Figure 11. The data point of the carrier concentration at 10 mm distance is slightly shifted horizontally to avoid overlap.

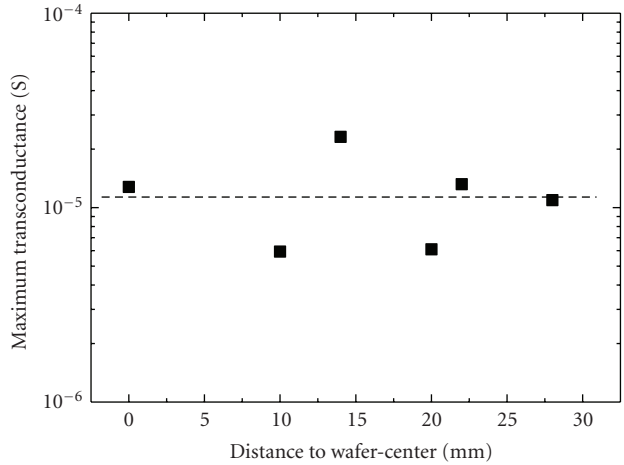

Figure 14: Variation of the best value of the maximum transconductance normalized to a width to length ratio of the different MESFET channels of 10.75 distributed over the 50 × 50 substrate of Figure 11.

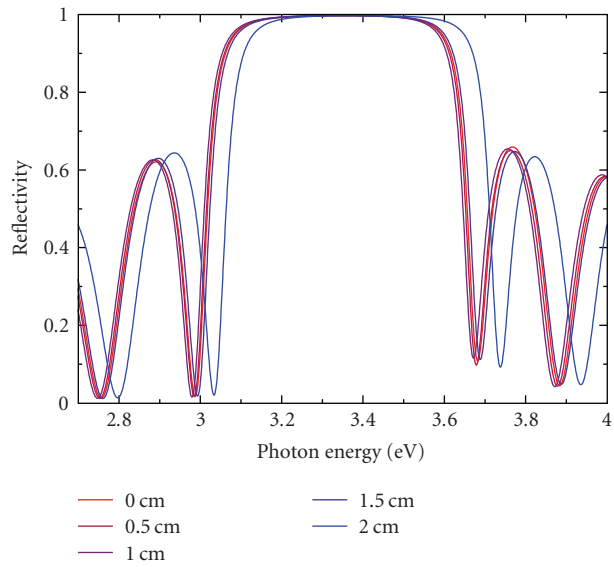

Figure 15: Five reflectivity spectra calculated using a layer stack model from the experimental ellipsometry data taken at the indicated radial positions on the 3-inch diameter Bragg structure on Si(100) wafer. The maximum reflectivity at the BR stop band energy with perpendicular incidence is 99.7%.

(that is also the plasma plume axis in propagation direction) to the center of the substrate, a laterally homogeneous deposition on large areas of 2-inch, 3-inch, or even 4-inch diameter is possible, as shown in paragraph 3.

2.3. Plasma Diagnostics with Optical Emission Spectroscopy. To get information on the optically excited species in the PLD plasma plume, we acquired optical emission spectra of the plasma plumes of several oxide materials [49] using a compact miniaturized optical spectrometer "Maya 2000 Pro" from Ocean Optics with a Hamamatsu back-thinned area CCD detector and USB interface. The spectrometer is equipped with a fixed HR composite grating with 300 lines per mm with variable-order filter to cover a wide spectral

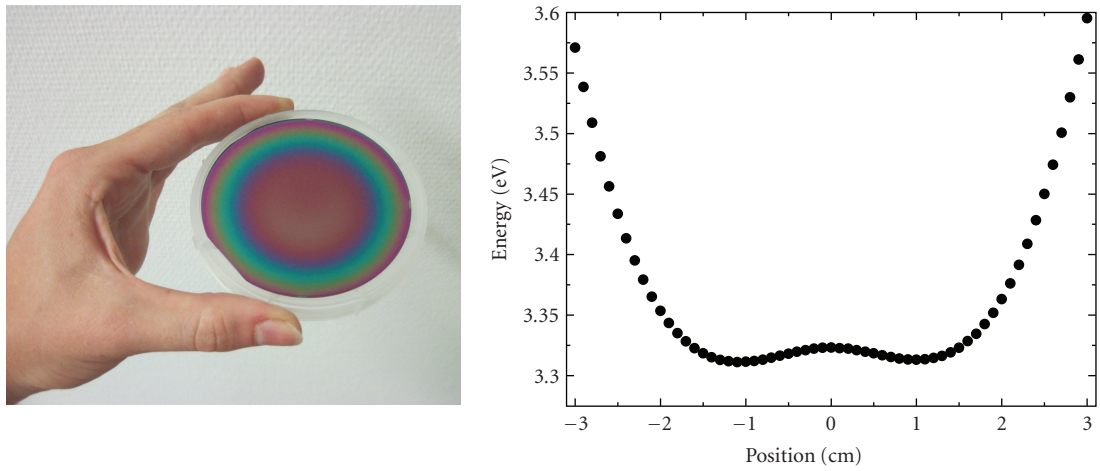

Figure 16: Photograph of the 3-inch diameter Al_2O_2/YSZ Bragg mirror on Si (100) (a) and radial scan of the center energy of the Bragg reflector stop bands (b). The position 0 cm is the wafer center. Within a diameter of 3 cm, the center energy is shifted by only 0.4% and within 4 cm diameter by 1.3%. The thickness of one layer pair is at the wafer center (0 cm) 93.3 nm, at 1 cm distance from center 93.6 nm, and at 2 cm distance 91.8 nm.

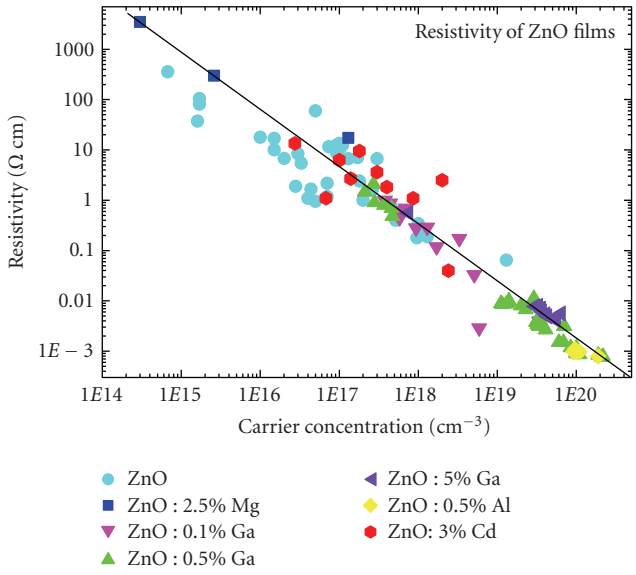

Figure 17: Typical resistivity and free carrier concentration of n-type conducting undoped ZnO, and Al-, Ga-, Mg-, and Cd-doped ZnO thin films on 10 × 10 mm^2 sapphire substrates taken from Hall measurements at 300 K and 0.4 Tesla. The given dopant concentrations are the initial concentrations in the PLD source targets. The line is drawn to guide the eye only. See [44] for additional information.

range from 200 to 1100 nm. The fixed spectrometer slit width is 10 μm, and for light collection we use a 400 μm UV-VIS optical SMA fiber and a Dynasil collimator lense. This collimator lense was combined with suitable viewports (7056 glass) of the PLD chambers (Figure 3) with direct view to the plasma plume (see Figure 4) for light collection. The viewport glass has usable transmission from about 250 nm to 2.5 μm. The spectra were taken always at a fixed position in the plasma plume of about 20 mm from the target surface. The spectra were averaged over 200 scans each with 100 ms integration time with a laser pulse repetition frequency of 10 Hz. With that, the resulting spectra are averaged over about 200 laser pulses. The software "Spectra Suite" was used to export the acquired spectra.

The aim of these investigations [49] was also to check if the optical emission spectra are suitable as input for a further sophisticated PLD process control to further enhance the stability and reproducibility of the PLD process. The dominating optical excitation mechanisms in the laser plasma are fluorescence (resonance) excitation due to absorption of the laser light, thermal excitation due to the high plasma temperature of several 1000 K, and shock excitation due to collisions with electrons and other atoms.

In the following we show typical optical emission spectra of our used oxide target materials. The peaks were identified by comparison with published data bases [51–53]. We identified emission lines of neutral atoms (called for Zn-atoms: Zn I), of single-ionized atoms (Zn II), and double-ionized atoms (called for oxygen atoms: O III). However, in our PLD plasma, similar to arc plasma with plasma temperature below 10,000 K, the emission from neutral atoms seems to dominate, as shown in Figures 5, 6, 7, and 8.

The process gas was found to have minor influence on the measured spectra, as we have shown for ZnO ablated in 0.1 mbar O_2 and N_2 (see [49], not shown here). Obviously, the optical plasma emission is mainly determined by the target material itself. The interaction with the background gas may become important at later stages of plasma expansion and with the film nucleation and growth. We checked also the dependence of plasma emission from the background gas pressure. However, at lower pressures of 0.01 to 0.0005 mbar

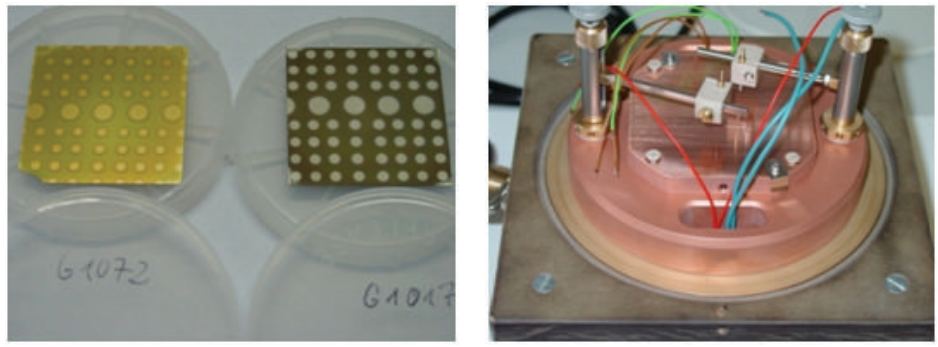

(a) (b)

FIGURE 18: (a) PLD $Ba_xSr_{1-x}TiO_3$ capacitor structures on microwave ceramic substrates (CoorsTek SUP 996 Hirel, 50 × 50 × 0.635 mm^3, A-face: $R_a \sim 21$ nm) with DC sputtered 3 mm diameter gold (G1072) or platinum (G1017) electrodes ~150 nm thick. The nominal thickness of the dielectric film is 1 to 2 μm. (b) Self-made temperature controller platform with adjustable top contacts for the large-area 50 × 50 mm^2 capacitor structures. The water cooled Peltier element enables a temperature sweep from −35°C up to +85°C.

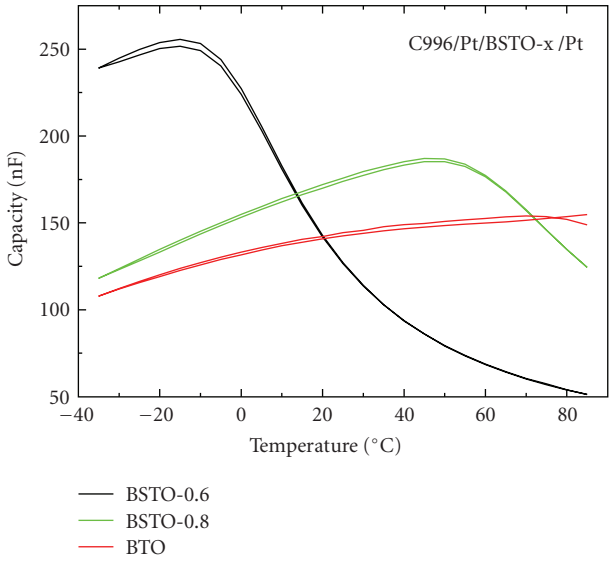

FIGURE 19: Temperature dependence of capacity $C = \varepsilon_0\varepsilon_r$ A/d (A is electrode area and d thickness of dielectric) of thin film capacitors, measured with 50 mV AC amplitude at 1 kHz and zero DC-bias. The dielectric was $Ba_{0.6}Sr_{0.4}TiO_3$ (BSTO-0.6, black line), BSTO-0.8 (green), and BTO (red). With decreasing Ba substitution, the ferroelectric Curie temperature (maximum of ε_r) increases. This structural phase transition is remarkably broadened due to the thin film nature of the dielectric. For C = 100 nF, d= 1 μm, and 3 mm circular electrodes, the relative permittivity ε_r of the dielectric is above 1,600.

the spatial extension of plasma changes considerably, and the emitted light intensities decrease. Therefore, all spectra shown here are taken at 0.1 mbar oxygen partial pressure, and the laser energy density at the target was 2 J/cm^2 using our KrF laser with 248 nm wavelength. Spectral lines from trace impurities in the targets were not found, as we used mostly 5N powders for target preparation. Figure 9 shows the OES spectra of undoped and Mn-doped zirconia which are surprisingly almost identical and which show a very high spectral density of lines.

3. PLD on Large-Area Substrates

Large-area PLD is demonstrated here for double-sided CeO_2/$YBa_2Cu_3O_{7-x}$ films on both sides of r-plane sapphire wafers up to 71 × 75 mm^2 size for microwave filter applications (Section 3.1.), for thin ZnMgO films on 50 × 50 mm^2 a-plane sapphire substrates for field effect transistor demonstrators (3.2.), and for large-area Bragg reflectors built from 10 double layers Al_2O_3/yttria stabilized zirconia (YSZ) with total thickness around 1 μm (3.3.). In addition, large-area ZnO- and $BaTiO_3$-based films are discussed in Sections 4.1. and 4.2., respectively.

3.1. Double-Sided High-T_c Superconducting $YBa_2Cu_3O_{7-x}$ Thin Films on 71 × 75 mm^2 Sapphire Substrates. The Leipzig development of a PLD process for double-sided deposition of CeO_2/$YBa_2Cu_3O_{7-x}$ (YBCO) on both sides of *r*-plane sapphire wafers began in 1992 and is described in [9–11, 43, 55–62]. The possible approaches for large-area PLD are demonstrated by Greer in [1, page 293 ff], and we adopted the so-called "off-axis" PLD, where the center of the large-area substrate holder and heater is laterally moved by the "off-axis" distance from the center of the PLD target and the axis of the plasma plume, as shown schematically in Figure 1 and in [61]. The "off-axis" distance has to be optimized together with the oxygen partial pressure to achieve the desired lateral homogeneity of film thickness and other physical properties. We have chosen the critical current density j_c at 77 K [56, 58] as measure for optimization of the large-area YBCO process. A high j_c is a necessary precondition for a low microwave surface resistance and a high microwave power handling capability [63]; see also [10]. Figure 10 shows the critical current density for two 71 × 75 mm^2 YBCO films on both sides of *r*-plane sapphire wafers, demonstrating a very good lateral homogeneity of

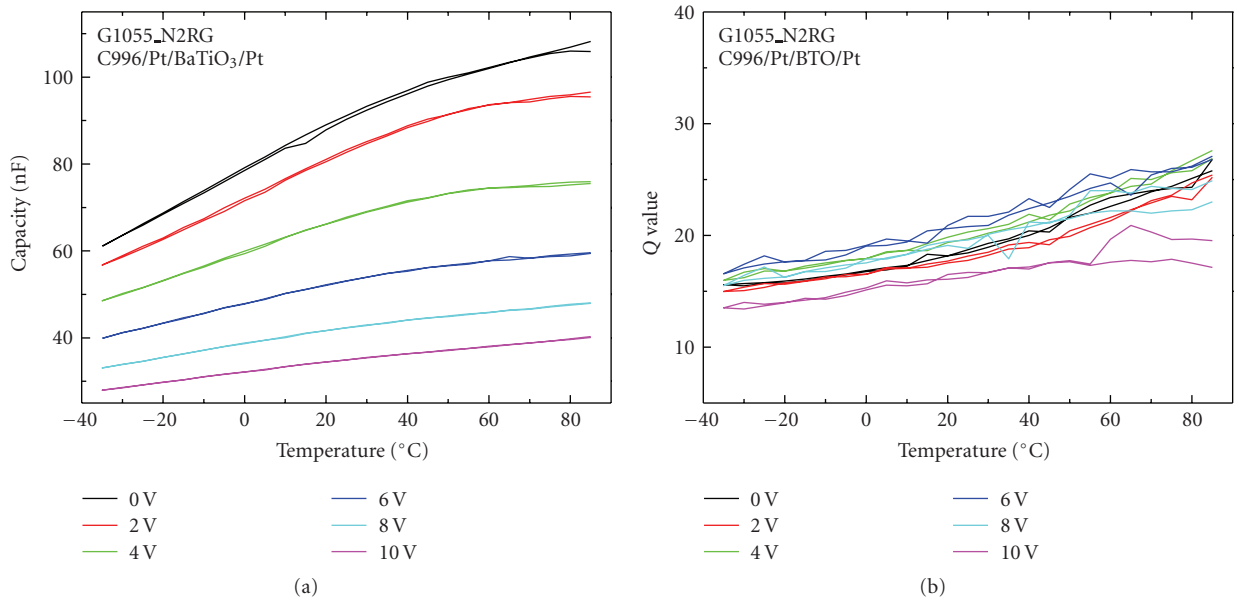

FIGURE 20: Capacity and Q value of an optimized $BaTiO_3$ thin film capacitor with Pt electrodes on CoorsTec microwave ceramic substrate in dependence on temperature and DC bias voltage (1 kHz). The relative tunability of capacity is shown in Figure 21. The Q value is maximum for 6 V DC bias.

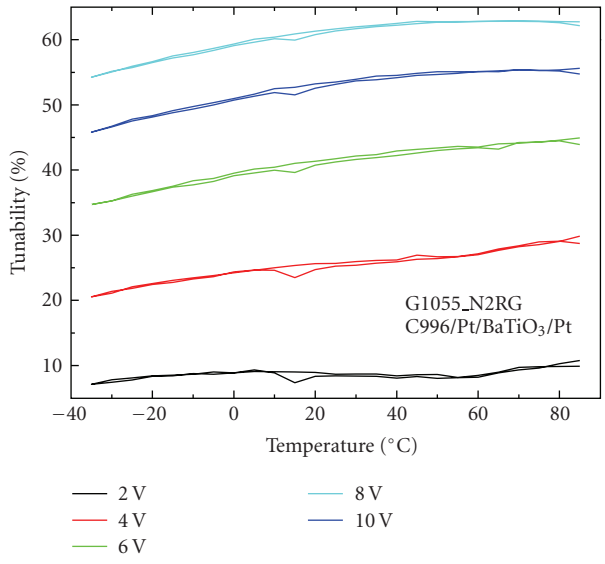

FIGURE 21: Relative tunability of capacity $(C_0 - C)/C_0$ in dependence on temperature and DC bias voltage for the BTO sample of Figure 20. The temperature dependence is weak as desired for applications. The tunability is 60% for electrical field strength in the dielectric of ~5 V/μm with an assumed thickness of 2 μm.

j_c as the most important quality criterion of the high-T_c superconducting thin films (Table 2).

Using these YBCO films (for sputtered and evaporated films see [64–67]), applications as low-loss microwave bandpass filters for multiplexers in future satellite communication systems or mobile communication base stations could be successfully demonstrated by the industrial project partners Robert BOSCH GmbH Stuttgart and Cryoelectra Wuppertal, respectively [68, 69]. Beside the development of the PLD growth itself, simple and effective characterization techniques are important. The inductive scan of the critical current density of high-T_c superconducting thin films called "j_c-scan Leipzig" [56, 58] is internationally successful with this respect.

3.2. ZnMgO Thin Films on $50 \times 50\ mm^2$ *Sapphire for Reproducible Field Effect Transistors.* Large-area ZnMgO thin films are deposited on double-side polished $50 \times 50\ mm^2$ a-plane sapphire substrates. The layers are intended for the channel in transparent metal-semiconductor field-effect transistors (T-MESFETs) [72, 73]. The PLD target was pressed from ZnO (5N) with 0.25 wt.% MgO (99,998%) and was sintered at 1150°C for 12 hours. The deposition was carried out using a 248 nm KrF excimer laser with pulse energy of 600 mJ. The substrate was heated to 670°C, and the oxygen pressure was kept constant at 0.02 mbar. The axis of the plasma plume touches the substrate at an "offset" distance of about 25 mm from the center.

In the following, investigations regarding the electrical homogeneity of films grown by PLD on such $50 \times 50\ mm^2$ substrates are presented. The substrate was cleaved after the deposition into 25 pieces of $10 \times 10\ mm^2$ size supported by a predefined line array at the wafer back side, as shown in Figure 11. The relative positions of investigated samples are given from the center of the small sample to the center of the uncleaved wafer.

The film thickness was determined ex situ by field-emission microscope cross sections prepared by focused ion beam milling using Ga-ions (see Figure 12). There is a slight

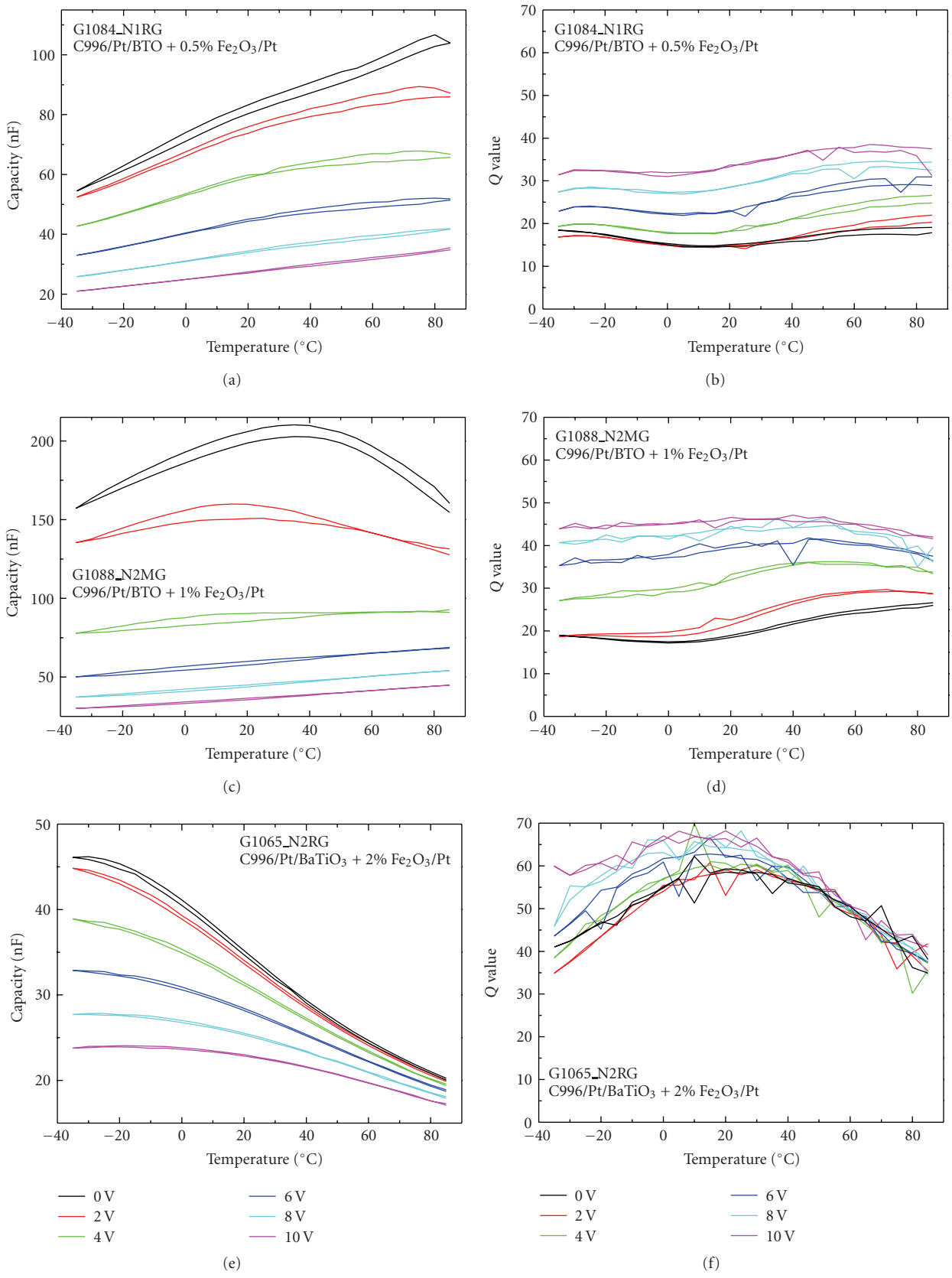

Figure 22: Effect of Fe doping of the BTO dielectric on capacity (a, c, e) and Q value (b, d, f) of Pt/BTO: Fe/Pt thin film capacitors for 0.5% (a, b), 1% (c, d), and 2% (e, f) Fe_2O_3 in the BTO PLD target. The dopant concentration influences the temperature dependence of permittivity considerably.

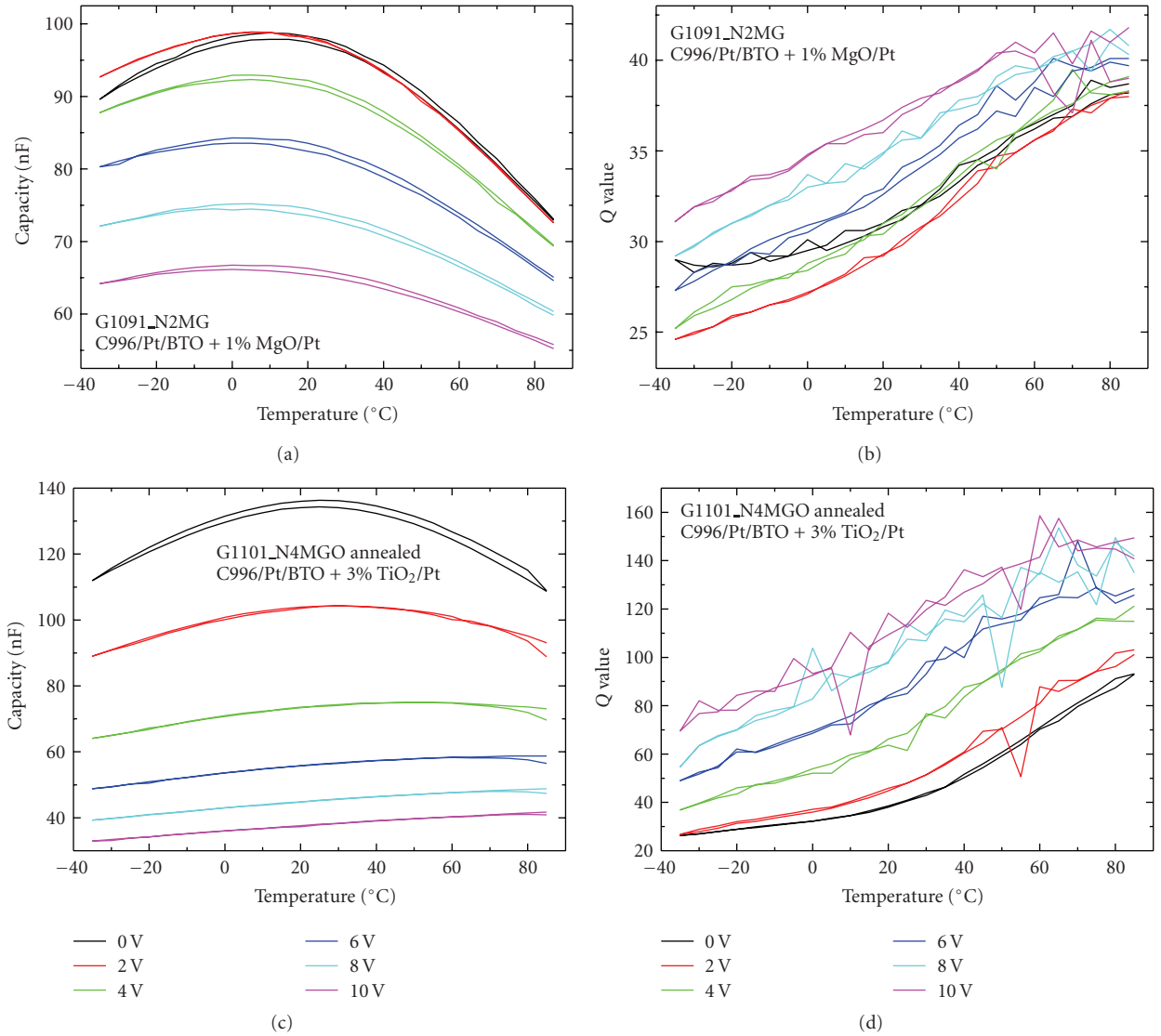

FIGURE 23: Effect of Mg (a, b) and Ti (c, d) doping of the BTO dielectric on capacity (a, c) and Q value (b, d) of Pt/BTO: Mg,Ti/Pt thin film capacitors. The Ti-doped capacitor (c, d) is postannealed in oxygen which improved the Q value by at least a factor of four.

reduction of the MgZnO layer thickness from the center to the edge of the wafer.

Hall-effect measurements reveal a homogeneous free carrier concentration of about 3×10^{18} cm^{-3} in the MgZnO thin film (Figure 13). Please note that such a high value is due to the diffusion of aluminium from the substrate, which acts as shallow donor [74, 75]. The Hall mobility does not vary significantly over the substrate radius and exhibits a value of about 20 cm^2/Vs (Figure 13). From this we conclude that the microstructural properties of the sample should be also laterally homogeneous.

The homogeneity of the MgZnO film is further demonstrated by the electrical properties of MESFETs fabricated on samples cleaved from different positions of the substrates as shown in Figure 11. For all MESFETs, the transfer characteristic (drain current versus gate voltage) was recorded for a drain voltage $V_D = 2$ V, and the maximum transconductance ($\max(dI_D/dV_G)$) was determined [72, 73]. For the purpose of comparison, the transconductance was normalized with the width to length ratio of the different MESFET channels (Figure 14). The best value of the maximum transconductance for each sample is depicted in Figure 14, revealing an almost constant value of about 1×10^{-5} S.

3.3. Bragg Reflectors on 3-Inch Diameter Si Substrates. Bragg reflectors (BRs) are wavelength selective highly reflective mirrors, made of periodic stacks of two transparent materials with different refractive indices but optical thickness of a quarter wavelength and are commonly used as one of the building blocks of microresonator structures [78, 79]. For various applications, it is desirable to vary the energetic distance between the optical and electronic mode in such resonators on one sample, but to maintain the properties of the Bragg reflector, especially its central wavelength.

Table 2: Typical microstructural and superconducting properties of double-sided 3-inch diameter PLD-YBCO films on sapphire with CeO_2 buffer layer [10]. Microwave measurements were done in Wuppertal [63] and Karlsruhe [70, 71].

Property	Typical value
YBCO-thickness d_{YBCO}.	(230 ± 30) nm
C-axis lattice constant c.	(11.659 ± 0.006) Å
A-axis lattice constant a.	(3.829 ± 0.003) Å
Orthorhombic splitting (b-a)/a.	(1.52 ± 0.05)%
Percentage of a-axis oriented grains.	0 to 0.5%
In-plane epitaxially oriented film area to total illuminated area in Raman spectroscopy.	75 to 94 %
Critical temperature T_c.	87.5 to 90 K
Critical current density j_c at 77 K and $B = 0$.	3.5 to 5.5 MA/cm^2
Surface resistance R_s at 10 GHz and 77 K.	500 to 600 $\mu\Omega$
Microwave surface magnetic field B_s at 8.5 GHz and 77 K for R_s + 20% [63].	8 to 10 mT
Surface resistance R_s at 145 GHz and 77 K [70].	40 to 60 mΩ

For this purpose, BRs consisting of 10 layers pairs of alumina and yttrium stabilized zirconia have been grown by PLD on 3″-Si wafers, applying an oxygen background pressure of 0.002 mbar and heating the substrate to 650°C. For more details of the growth and optical properties of such Bragg reflectors, see [43, 78, 80]. To achieve homogeneous large-area BR, the substrate holder was placed far off the center of the plasma plume, near the wafer edge, and was rotated with 9 rpm. The average thickness of one-layer pair and of the whole BR structure within 2 cm distance from the wafer center is 93 nm and 930 nm, respectively.

Figure 15 shows reflectivity spectra, calculated for normal incidence from a layer stack model obtained by transfer-matrix analysis of the ellipsometry data. The maximal reflectivity of the BR stop-bands is 99.7%. The central wavelength respective photon energy shifts from 3.32 eV in the wafer center via 3.31 eV to 3.36 eV at the radial distance of 2 cm (Figure 16). In an area of diameter of 3 cm, the central wavelength varies less than 0.4%. The energy shift corresponds to the changing layer thickness at the wafer edge, as visualized by the color gradient in the photograph in Figure 16.

4. Controlled Doping of Oxide Thin Films

As mentioned above, the unique flexibility of PLD concerning the deposited material is one of its outstanding advantages. Here we show examples for doping and alloying of ZnO thin films for future optoelectronic applications (Section 4.1), and for doped $BaTiO_3$ thin films with optimized dielectric properties within a certain temperature range (Section 4.2). Because trace impurities may influence considerably the desired effect of doping as, for example, the demanding p-type conductivity of the ZnO semiconductor thin films, we include trace element analyses of PLD targets and films in the discussion in Section 4.1.

4.1. Doping of ZnO Thin Films to Control Their Electrical Properties. A variety of dopants have been investigated in PLD ZnO films, as shown in Table 5 and in [44, 81–92]. The addition of the dopants is done simply by mixing the dopant element in form of the appropriate oxide into the ZnO powder used for PLD target preparation [6]. By ball milling the powder mixture, a homogenous distribution of the dopant will be achieved. Because the mill beaker and balls are one of the possible sources of unintentional trace impurities, we investigated the effect of three different beaker and ball materials, namely, silica (agate), zirconia and tungsten carbide (Table 6). After pressing the powder in a hardened stainless steel compression mould, the ZnO-based targets will be sintered at 900 to 1,150°C in air for 12 h in a furnace. In the PLD process, deviations of the film composition from the initial target composition may occur because of the particular chemical properties of ZnO and the dopants, as for example, evaporation temperature and dopant solubility in the ZnO matrix. Table 5 summarizes the average composition transfer factors from the PLD target into the grown film. The film compositions were analyzed by ion beam analysis using combined Rutherford backscattering spectrometry (RBS) and particle-induced X-ray emission (PIXE) with 2 MeV He^+ and 1.2 MeV H^+ ions, respectively [93]. For most dopant elements, a transfer factor above 1 was determined (Table 5). That means that the chemical composition of the dopant element in relation to Zn is increased by the PLD process. The element with the lower evaporation temperature (mostly Zn) may evaporate preferably from the heated substrate due to the lower sticking coefficient, thus yielding a lowered composition of this particular element in the film. However, some dopant elements, as P [86], Ni, and Cu, and Cd [44, 92], show transfer factors considerably below 1. Here, P and Cd show lower evaporation temperatures as compared to Zn, thus explaining the low transfer factors of these elements into the ZnO-based films. In addition, a low solubility of CdO in ZnO of a few at. % is reported [44, 92], thus explaining the extremely low transfer factor of Cd. However, the correlation of low transfer factor and low evaporation temperature does not apply for Ni and Cu as neighbor elements to Zn in the periodic system.

In contrast, Mg has the highest transfer factor of all dopant elements [44, 87–89]. Probably, the preferential ablation of ZnO out of the MgZnO target is an additional reason for the Mg-enriched films because of the low optical absorption coefficient of MgO with E_g around 8 eV for the excimer laser light at 248 nm wavelength. The observed continuous shift of the MgZnO film composition with the ablation state of the MgZnO target [41] supports this assumption of the preferential target ablation.

Table 3: Relative permittivity and loss tangent of typical large-area $Ba_xSr_{1-x}TiO_3$ thin films grown by PLD or sputtering on the indicated substrates (size $50 \times 50\,mm^2$ or 2-inch diameter), measured at 35 GHz and 300 K with an open Fabry-Perot resonator by R. Heidinger at Karlsruhe Research Center. The BSTO films grow with polycrystalline structure on the ceramic substrates and with oriented epitaxial structure on the single-crystalline substrates.

Growth method	Substrate	$Ba_xSr_{1-x}TiO_3$-film	Thickn.	ε_r	$\tan\delta$
PLD (U Leipzig)	CoorsTec *	$Ba_{0.45}Sr_{0.55}TiO_3$ (poly)	500 nm	1140–1640	(0.3 bis 0.8) $\times$ 10^{-2}
PLD (U Leipzig)	CoorsTec *	$Ba_{0.6}Sr_{0.4}TiO_3$ (poly)	500 nm	720	5×10^{-2}
PLD (U Leipzig)	LTCC *	$Ba_{0.7}Sr_{0.3}TiO_3$ (poly)	390 nm	500	30×10^{-2}
PLD (U Leipzig)	r-sapphire	$Ba_{0.7}Sr_{0.3}TiO_3$ (110)	130 nm	900–1150	35×10^{-2}
PLD (U Leipzig)	$LaAlO_3$	$Ba_{0.7}Sr_{0.3}TiO_3$ (100)	180 nm	1300–1600	50×10^{-2}
sputtering (FZK)	$LaAlO_3$	$Ba_{0.7}Sr_{0.3}TiO_3$ (100)	200 nm	500–550	(7 to 9) $\times$ 10^{-2}

* Al_2O_3-based polycrystalline microwave ceramics. The surface roughness R_a of the LTCC-substrates was 95 to 145 nm, and R_a of the CoorsTec substrates 21–27 nm (A-face HIREL quality).

Table 4: XRD ω-scan width of ZnO (0002) peak, PL-D^0X_A FWHM, Hall mobility μ_H, and carrier concentration n of a series of ZnO thin films grown by the indicated multi-step PLD process on c-plane sapphire substrate. The nucleation and intermediate layers are always 30 nm, and the main layers are 1,200 nm thick. The thin nucleation and interlayers are grown at 600°C and the thick ZnO layers at 1.5×10^{-2} mbar oxygen partial pressure and 750°C growth temperature [102].

PLD steps	XRD ω-scan ZnO(002) (arsec)	FWHM PL-D^0X_A(2 K) (meV)	μ_H (cm^2/Vs) (300 K)	n (cm^{-3}) (300 K)
One-step	446	3.2	30	5×10^{17}
Two-step high temp. *	320	2.4	60	1.4×10^{16}
Two-step	338	2.2	141	5.4×10^{16}
Three-step	241	2.0	119	2.8×10^{16}
Four-step	256	1.9	101	7.5×10^{15}

* 750°C growth temperature for the thin nucleation layer, instead of 600°C at the other processes.

Figure 17 shows the resistivity and carrier concentration range of nearly 7 orders of magnitude that can be reached by doping of ZnO films with Mg, Ga, Cd, and Al, in addition to undoped ZnO thin films. The optimized undoped ZnO films show lower intrinsic carrier concentration. The carrier concentration and resistivities were determined by Hall measurements in Van der Pauw geometry with sputtered Au-contacts at the corners of the $10 \times 10\,mm^2$ films.

To get a first estimate on the trace element contamination of the PLD ZnO films, we analyzed three MgZnO targets prepared in different ball mills (Table 6) and two undoped ZnO thin films (Table 7) for their trace element concentration by PIXE/RBS [93]. The results of Table 6 show the minor effect of the material of the grinding beaker of the used ball mill for homogenising the initial powders in the PLD target preparation. Within the detection limits of the PBS-PIXE analysis, no remarkable differences for the three beaker materials were found. The MgZnO films grown from these three targets are investigated by capacitance-voltage spectroscopy and thermal admittance spectroscopy, but no remarkable difference of free carrier concentrations and defect levels is obtained up to now.

For most elements listed in Table 7, the detected trace element concentrations in the large-area ZnO films are below the given detection limits of the ion beam analysis. At the edges of the 32.8 mm diameter wafers, remarkable concentrations of the elements K, Ca, Ti, Cr, and especially Fe were found. Most of these elements are constituents of stainless steel, and the stainless steel substrate holder and the hot parts of the substrate heater in the PLD chamber are most probably the source of the Fe and Cr contamination at the film edges. In the center of both investigated films, the impurity concentrations of nearly all elements are near

Table 5: Selection of dopants for ZnO and the aim of doping, together with transfer factors of dopant composition from the PLD target into the thin film, as determined by RBS and PIXE analysis of at least five different films for each dopant [6, 93]. DMS stands for diluted magnetic semiconductor which is still challenging, as well as stable and reproducible p-type conductivity in ZnO.

Dopant in ZnO	Aim of doping	Transfer factor from target into thin film
Li	p-type conductivity	1.37 ± 0.72
N	p-type conductivity	N/A
Mg	higher band gap	1.86 ± 0.49
Al	n-type conductivity	1.56 ± 0.44
P	p-type conductivity	0.50 ± 0.01
Ti	DMS	1.15 ± 0.43
Mn	DMS	1.03 ± 0.28
Fe	DMS	1.47 ± 0.16
Co	DMS	1.23 ± 0.09
Ni	DMS	0.15 ± 0.02
Cu	DMS	0.74 ± 0.25
Ga	n-type conductivity	1.54 ± 1.04
Cd	lower band gap	0.09 ± 0.12
Sb	p-type conductivity	1.71 ± 0.32

Table 6: Typical RBS and PIXE trace element concentrations in ppm (2,0 MeV H^+; ∅ 0,4 mm; 50 μC) of three ZnO+2%MgO PLD targets prepared from 99.995% ZnO and 99.998% MgO powders. The initial powders were homogenized in ball mills with three different grinding beakers, as indicated in the first column. Obviously, there is nearly no influence of the beaker material on the trace element impurities within the detection limits. Concentrations with "<" are below the detection limits of the analysis; for Si the detection limit is ~300 ppm, similar to tungsten.

ZnO+2% MgO targets milled in:	Ti	Cr	Fe	Co	Ni	Zr	W
WC beaker	17 ± 5	15 ± 4	36 ± 6	<14	<24	<49	<317
ZrO_2beaker	15 ± 5	<5	42 ± 6	<14	<23	<46	<309
SiO_2 beaker front side*	12 ± 4	<5	47 ± 7	<14	<24	<49	<321
SiO_2 beaker back side*	16 ± 5	<5	52 ± 7	<14	<24	<47	<319

*Front and back side refers to the side of the PLD target. Front side was ablated already for film growth.

Table 7: Typical atomic concentrations of trace elements from combined PIXE/RBS analysis with 1.2 MeV protons (all values given in ppm) of two large-area 32.8 mm diameter ZnO thin films on sapphire. The PLD target was sintered from 99.9995 at.% ZnO powder. Films were grown with stainless steel substrate holder at growth temperature of about 650°C. Therefore, the Fe concentration is much higher at the wafer edges. Most elements are below the detection limits.

Sample*	Si	K	Ca	Ti	V	Cr	Mn	Fe	Ni	Cu
E391 c	1,342	<16	24	<11	<14	<15	20	35	<67	<153
E391 e	<901	30	28	<13	<16	28	<19	1,069	<69	<166
E392 c	<971	<30	<24	<21	<24	50	<26	<33	<104	<215
E392 e	<1,272	54	51	27	<29	85	41	206	<103	<243

*Sample no. E391 and E392, c and e stand for center and edge analysis position on the wafer, respectively.

or below the detection limit of the ion beam analysis, thus demonstrating the high potential of PLD to deposit films with low concentration of unintentional trace elements. The concentration of Fe, Cr, and Ni can be further reduced by the use of a substrate holder made of molybdenum instead of stainless steel, as we have shown in recent investigations of defect-induced ferromagnetism in ZnO [94].

More detailed information about the very broad ZnO research activities of the Semiconductor Physics Group in Leipzig which is based on PLD ZnO thin films and nanostructures can be found in Sections 3.2, 5.1, and 5.2, and 6.1. of this paper, and at the homepage www.uni-leipzig.de/~hlp/, and in [6, 43].

4.2. Doped $BaTiO_3$ Thin Films with Optimized Temperature Dependence of Dielectric Permittivity. Doped and undoped ferroelectric $BaTiO_3$ (BTO) and $Ba_xSr_{1-x}TiO_3$ (BSTO) thin films were investigated in cooperation with the industrial partners Robert Bosch GmbH (Stuttgart) and Marconi Communications (Backnang) to demonstrate electrically tuneable ferroelectric microwave devices for automotive distance radars and for directional radio applications, respectively. Voltage-controlled varactors may tune oscillators, filters, phase shifters, delay lines, and antennas [95, 96]. As substrate material for the film growth we had to use polycrystalline, Al_2O_3-based microwave ceramic plates with 50 × 50 mm^2 (CoorsTek, see Figure 18). The working temperature range of the device structure was set to −35°C up to + 85°C. The homogeneity of the dielectric properties within this temperature range was controlled on one hand by the Ba- to Sr-composition ratio in the mixed compound $Ba_xSr_{1-x}TiO_3$ (e.g., BSTO-0.8 stands for $x = 0.8$) [97], and on the other hand by doping of the BTO films by metal oxides. There are some indications in the literature that doping of BTO with Mg, Al, La, and Ta reduces the losses (Q-factor) but also the relative permittivity ε_r [98].

In our work, we have partially substituted the Ba and Ti within the $BaTiO_3$ by Sr and Zr, respectively, to obtain BSTO-0.6, BSTO-0.8, and $BaTi_{0,8}Zr_{0,2}O_3$. Furthermore, we have doped $BaTiO_3$ with 1% and 2% MgO, 1% and 2% Y_2O_3, 3% TiO_2, and 0,5%, 1%, 2%, and 5% Fe_2O_3, employing the unique materials flexibility of PLD. All substitutes and dopants were mixed as oxides directly into the PLD targets. The dielectric permittivity ε_r and the loss tangent $\tan\delta$ were measured at low frequency of 1 kHz using thin film capacitors in the temperature range −35°C up to + 85°C. The capacitors consist of a DC-sputtered Au or Pt ground film (200 nm) at the smoother side of the above-mentioned microwave ceramic substrates. The doped BTO and BSTO films were PLD grown [97], and on top was sputtered the upper Au or Pt capacitor electrode using shadow masks, as shown in Figure 18(a). An RCL meter Fluke 6306 and a temperature platform with a Peltier element (see Figure 18(b)) were used for the capacitor measurements at 1 kHz with 20 mV or 50 mV AC-amplitude and DC bias 0–10 V. This measurement gives also the Q-factor as the ratio of capacitive to Ohmic resistance, which is roughly equal to the inverse loss tangent $\tan\delta$.

The results of the low frequency investigations are shown in Figures 19, 20, 21, 22, 23, and in Table 8. Figure 19 shows the effect of Ba substitution by Sr on the temperature dependence of the capacity and permittivity at 1 kHz. The permittivity maximum shifts to higher temperature with decreasing substitution. For typical capacity of C = 100 nF, typical thickness of the dielectric of $d = 1\,\mu$m, and 3 mm circular top electrode the relative permittivity ε_r of the dielectric films is above 1,600; see Figures 19, 20, 21, 22, and 23, and for corresponding microwave data, see Table 3. Because of the rough substrate surface, the effective thickness of the dielectric is hardly to determine for each particular capacitor. Figure 20 shows the capacity and Q value of a $BaTiO_3$ thin film capacitor with Pt electrodes in dependence on temperature and DC bias voltage (1 kHz). The tunability of capacity by the DC voltage of the same structure is shown in Figure 21 and is nearly independent of temperature from −35°C up to 85°C.

Doping and postannealing effects on the dielectric properties of BTO thin films are demonstrated in Figures 22 and 23. Increased doping with Fe reduces the losses,

Table 8: Overview of doping dependence of dielectric properties of planar $Ba_xSr_{1-x}TiO_3$:M (M = Fe, Mg, Y, Ti, Zr) thin film capacitors on microwave ceramic substrates. Maximum values of capacity at zero DC bias, *Q* value, and tunability are highlighted by bold type. See Figures 19, 20, 21, 22, and 23 for the sample design and selected, more detailed graphs of C and *Q* as functions of T for DC bias from 0 to 10 V.

PLD thin film dielectric in Pt-BSTO:X-Pt capacitor	Capacity [nF] @ 0 V and 20°C	*Q* value @ 0 V and 20°C	Tunability ΔC/ΔU [nF/V] for ΔU = 10 V @ 20°C	T-coefficient ΔC/ΔU [nF/K] @ 0 V, ΔT = 25°–15°C
Undoped BSTO:				
BTO	89	18	5.5	0.44
BSTO-0.8	**172** (5 V)*	17 (5 V)*	**20.7**	0.77
BSTO-0.8 annealed	**116**	**42**	7.8	0.46
BSTO-0.6	**195** (5 V)*	29 (5 V)*	**24.7**	–4.6
BSTO-0.5 to 0.85 Gradient H. Christen, ORNL, USA	**112** (5 V)*	22 (5 V)*	**10.5**	–1.14
Doped BTO:				
BTO:Fe_2O_3(0.5%)	83	15	5.6	0.41
BTO:Fe_2O_3(1%)	**206**	18	**17.0**	0.49
BTO:Fe_2O_3(2%)	35	**58**	1.2	–0.3
BTO:Fe_2O_3(5%)	24	**49**	0.4	–0.11
BTO:MgO(1%)	98 (5 V)*	31 (5 V)*	6.6	–0.08
BTO:MgO(2%)	40 (5 V)*	14 (5 V)*	0.5	–0.08
BTO:Y_2O_3(1%)	49	17	2.9	0.19
BTO:Y_2O_3(2%)	**149**	18	**12.2**	0.39
BTO:Y_2O_3(2%) annealed	**118**	**26**	**9.4**	0.43
BTO:TiO_2(3%)	90 (5 V)*	23 (5 V)*	9.0	–0.003
BTO:TiO_2(3%) annealed	**136**	**38**	**9.8**	0.09
$BaTi_{0.8}Zr_{0.2}O_3$	78	24	5.5	–0.6

*For these samples the maximum DC bias was 5 V, because of the leackage currents.

but influences considerably the temperature dependence of permittivity; see Figure 22 and [97]. Other metal dopants change the temperature dependence of capacity (ε_r) and of the *Q*-value in different ways, as Figure 23 and Table 8 show. Annealing steps reduce remarkably the loss (*Q*-value) but the permittivity remains nearly unchanged; see Figure 23 and Table 8. A summary on all investigated substitutes and dopants is given in Table 8, together with the low frequency dielectric properties of the thin film capacitors. The highest values of permittivity (capacity), *Q* value, and tunability are marked in red in Table 8. Obviously, high Sr-substitution and Fe-doping [97] promote a high permittivity.

In addition, the dielectric properties were measured at microwave frequency of 35 GHz for selected large-area BSTO films without any metal electrode by Heidinger using an open Fabry-Perot-resonator at Karlsruhe Research Center similar to that in [70, 71]. Table 3 shows the results for $Ba_xSr_{1-x}TiO_3$ films with x = 0,45, 0,6, and 0,7. For these measurements, the BSTO films were grown without any metal electrode on different substrates as mentioned in Table 3. With decreasing Ba-content (increasing substitution by Sr), the relative permittivity increases, and the losses are reduced simultaneously. In addition, the growth parameters influence the dielectric microwave properties. Large-area PLD films show high microwave permittivities clearly above

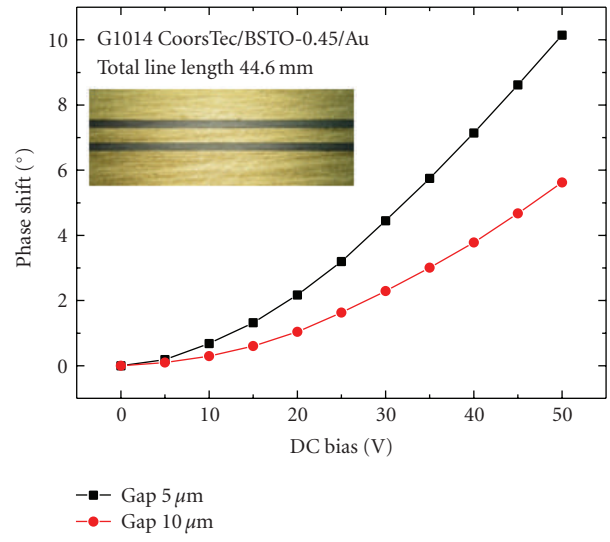

Figure 24: Phase shift at 10 GHz by transmission through a coplanar microwave line (made of gold) on BSTO-0.45 thin film at 25°C. The line width is 200 μm, and the gap to the grounded areas is 10 μm (red curve) and 5 μm (black curve); see inset. The Curie temperature of BSTO-0.45 is below −50°C and therefore shows a weak tunability of phase shift at +25°C.

1,000. Based on these investigations, the PLD BSTO thin films were used for planar microwave components and for phase shifter demonstrators (see Figure 24) in cooperation with Marconi Communications Backnang.

Microwave investigations of ferroelectric thin films are of current international interest; see for example the overview on tunability and dielectric losses of STO, BSTO, and BTO thin film heterostructures and bulk materials [99]. A "616 element scanning phased array antenna" based on 48 two-inch diameter BSTO-0.5 films on LAO was presented by the NASA Glenn Research Center [100]. This antenna system includes 616 identical phase shifters for 19 GHz. The average relative permittivity of the BSTO-0.5 films was 2,129 with a standard deviation of 149 [100]. A current research subject is the strain engineering of the dielectric properties of ferroelectric BTO films [101].

5. ZnO Films with Low Dislocation Density

By the introduction of low-temperature interlayers, we were able to reduce the dislocation density in heteroepitaxial ZnO thin films on c-sapphire to achieve high Hall mobilities above 150 cm^2/Vs at 300 K (Section 5.1.). ZnO homoepitaxy is a further possibility to grow films with very low dislocation density and corresponding high Hall mobilities up to 800 cm^2/Vs below 100 K (Section 5.2.).

5.1. Multistep PLD of ZnO on C-Sapphire with High Hall Mobility. A multistep PLD process was developed to grow nominally undoped ZnO thin films on c-plane sapphire with thickness of 1 μm to 2 μm using low-temperature nucleation and intermediate layers between the high-temperature grown ZnO main layers [102]. The multi-step grown ZnO thin films on c-plane sapphire exhibit high Hall mobilities of more than 150 cm^2/Vs at 300 K. The key issue of this multistep PLD process is the insertion of 30 nm thin ZnO relaxation layers grown at reduced substrate temperature as shown in Table 4; see also [102] for further details.

The high-mobility samples show atomically flat surface structure with grain size of about 0.5 $-$ 1 μm, whereas the surfaces of low-mobility films consist of hexagonally faceted columnar grains of only 200 nm size in the atomic force microscopy images [102]. Structurally optimized PLD ZnO thin films show narrow photoluminescence line widths of donor bound exciton of 1.7 meV at 2 K. The concept of nucleation and intermediate layers grown at lower temperature as compared to the main functional layer was first proposed by Amano et al. for GaN films [50] and was transferred successfully to the ZnO system [102]. Obviously, the low temperature layers compensate lateral strain and reduce the number of dislocation lines in growth direction, as shown in the TEM cross section in Figure 25.

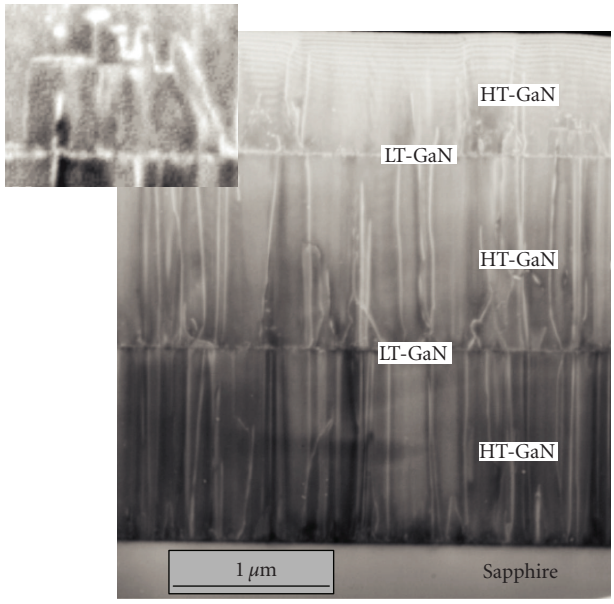

Figure 25: TEM dark field cross-section of an MOCVD GaN structure on c-sapphire with low temperature LT-GaN buffer layer at the sapphire/GaN interface and two low temperature GaN interlayers in between the high-temperature HT-GaN layers. The number of dislocations clearly decreases in growth direction from bottom to top. The inset at the top left shows a dislocation half loop formed in the HT-GaN layer in the vicinity of an LT-interlayer. Obviously, the interlayers act as barriers for the propagation of dislocations. Adapted from Benamara et al. [50].

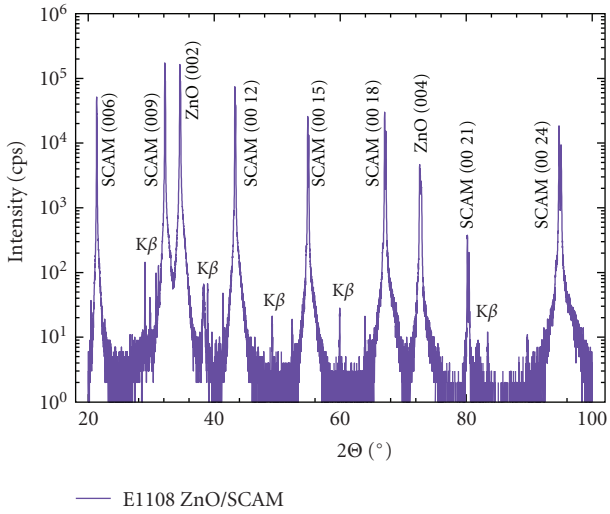

Figure 26: XRD wide angle $2\Theta - \omega$ scan (Cu K_α) of a PLD ZnO thin film on a $ScAlMgO_4$ (006) substrate.

5.2. ZnO and ZnMgO Thin Films on Lattice Matched Substrates. High-quality light emitters and other electronic and optoelectronic devices require ZnO thin films with very high structural quality. One way to reduce the dislocation density in thin films is to reduce the lattice mismatch of film and underlying substrate. Sapphire and ZnO show in-plane lattice mismatch above 10%, and these ZnO films show a high mosaicity with small-angle tilted grains and a high density of dislocations which decrease the electrical performance of the films. A better lattice-matched substrate to ZnO is $ScAlMgO_4$ (SCAM) with nearly identical in-plane

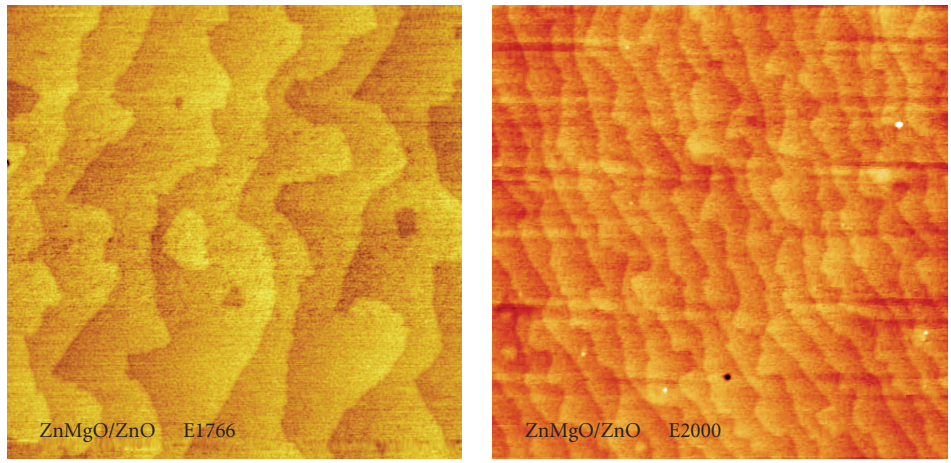

(a) (b)

FIGURE 27: AFM surface images of $Zn_{0.96}Mg_{0.04}O$/ZnO quantum well/$Zn_{0.96}Mg_{0.04}O$ films on ZnO (0001). The scan size is $2\,\mu m \times 2\,\mu m$, and the z-scales are 2.16 nm (E 1766) and 2.5 nm (E 2000). ZnMgO monolayer terraces with step height c or c/2 corresponding to two-dimensional layer by layer growth are visible. The total film thickness and the out-of-plane strain are 380 nm and 330 nm and −0.18% and −0.22% for E1766 and E2000, respectively [54].

a-lattice constant of 3.236 Å (a_{ZnO} = 3.2501 Å). Figure 26 shows an XRD $2\Theta - \omega$ scan of a PLD ZnO thin film on SCAM. Due to the much better lattice match, ZnO on SCAM (006) shows considerably reduced ZnO(002) rocking curve width as compared to ZnO on sapphire (Table 9). However, SCAM is an expensive material, and the SCAM substrates show a strongly anisotropic layered morphology with laterally not homogeneous structural properties, as we have found for the tilt mosaicity.

Only recently, ZnO single crystals became commercially available for a reasonable price, and ZnO homoepitaxy could be performed. We have demonstrated the PLD of undoped ZnO thin films with high structural quality [103] on thermally pretreated hydrothermal O-face ZnO single crystals. Details of the ZnO substrate preparation, the homoepitaxial PLD growth, and the preparation of the TEM cross sections can be found in [103–105]. The electrical and optical properties of homoepitaxial ZnO films doped with about 0.01% phosphorus are reported in [105, 106]. Interestingly, such as-grown ZnO:P and ZnMgO:P thin films are highly n-type conductive [54, 105–107], which is in partial agreement with [108–110]. More structural properties, in particular detailed HR-XRD and TEM investigations of undoped and phosphorus doped homoepitaxial ZnO and ZnMgO thin films, were reported in [54, 104].

Selected MgZnO:P films showed an annealing-induced increase of the resistivity of nearly 10^6; however, the films were still n-type. ZnO:P films (without MgO) showed a much smaller annealing effect [54, 107]. This is in contradiction to heteroepitaxial ZnO:P films with more structural defects, which could occasionally be switched from n-type into p-type [108–110]. Preliminary evidence for a formation of a two-dimensional electron gas in homoepitaxial MgZnO-ZnO-MgZnO quantum well structures is shown in [111].

TABLE 9: Full width at half maximum (FWHM) of HR-XRD ZnO(002) rocking curves of PLD ZnO and ZnMgO thin films on the indicated substrates (best values). ω-scans were taken with Cu $K_{\alpha 1}$ radiation and with open detector at the 2Θ position of ZnO(002). For details see [54, 104].

Film on substrate (sample no.)	FWHM of HR-XRD rocking curve of ZnO(002) film peak
ZnO on a-sapphire (E1105)	369″
ZnO on n-GaN/c-sapphire (E1111)	305″
ZnO on c-sapphire (multistep PLD)	151″
ZnO on $ScAlMgO_4$(006) (E1108)	71″
ZnMgO on ZnO(0001) (E2064)	27″
ZnO on ZnO(0001) (E1340)	23″ (no peak separation)

In [54], we extended the detailed structural investigations in [104] to homoepitaxial ZnO films alloyed with Mg (0 to 4%) and doped with P (0 to 1%). In particular, a complete survey on Hall data of grown MgZnO:P films is given. The ZnMgO films show atomically flat surfaces with monolayer steps of c/2 or c in the atomic force microscopy (AFM) images (Figure 27). Two-dimensional growth with terrace-like surface structure is most prominent for the Mg-alloyed films without P. Transmission electron microscopy (TEM) and high-resolution X-ray diffraction (HR-XRD) confirm a very low dislocation density (Figure 28) and narrow rocking curves of undoped homoepitaxial ZnO films grown by PLD (Table 9). ZnO(002) rocking curves of $Zn_{95.99}$ $Mg_4P_{0.01}$ O films on ZnO(001) were as narrow as 27 arcsec with an FWHM of the substrate peak of 23 arcsec. Extensive HR-XRD triple-axis scans are reported with special attention to samples which show a clear splitting of film and substrate peaks in XRD [54]. For these samples, c-axis and a-axis lattice constants were determined

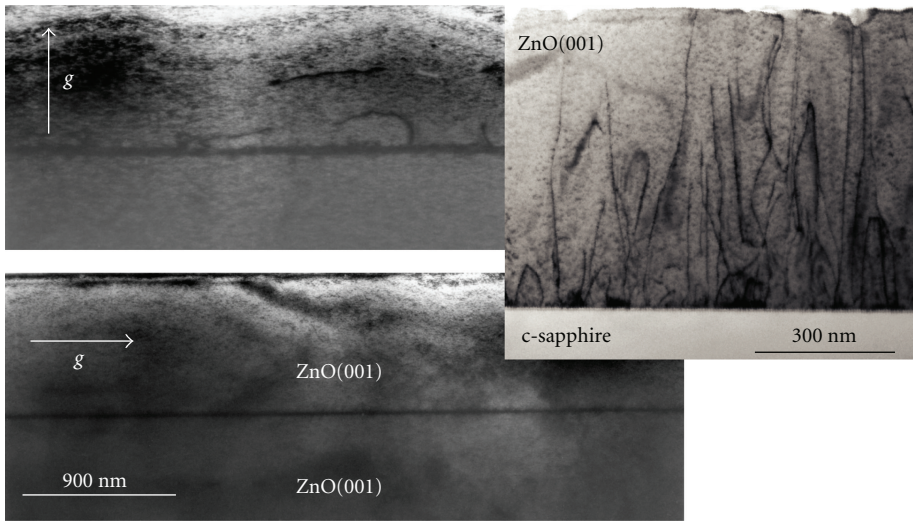

Figure 28: TEM bright field (11.0) cross sections of homoepitaxial undoped ZnO film E1289 taken with two different g-vectors (left), taken by Wagner (see [54]). The few dislocations for g-vector in c-direction are out of contrast for $g = [-11.0]$, therefore their Burgers vectors are of c-type. The film thickness is 893 ± 5 nm, as determined from the intensity oscillations in the HR-XRD $2\Theta - \omega$ scan (not shown here). The right inset (provided by W. Mader, Bonn) shows for comparison a heteroepitaxial PLD ZnO film on c-plane sapphire E435 with much higher dislocation density, in particular near the interface.

independently for homoepitaxial film and underlying ZnO substrate. In-plane lattice-matched, pseudomorphic growth with compressive or tensile strain was confirmed for all investigated samples. Figure 29 shows triple axis $2\Theta - \omega$ scans of the ZnO(002) peaks of two selected samples which show tensile or compressive film strain. The results show the balance between tensile strain induced by Mg and compressive strain by P in ZnO [54]. The in-plane lattice-matched, pseudomorphic growth mode of these two tensile or compressively strained films is demonstrated by reciprocal space maps of the asymmetric (104) reflections in Figure 30. High electron mobilities up to 190 cm^2/Vs at 300 K and up to 800 cm^2/Vs at 70 K were found in the homoepitaxial MgZnO:P thin films [54, 105–107]. The effect of a further increase of the Mg concentration in homoepitaxial ZnMgO films up to 22 at% on the structural and optical properties is demonstrated in [112]. The corresponding HR-XRD RSMs show an increasing tilt mosaicity and the loss of lattice matched growth with increasing Mg content [112]. However, the homoepitaxial film with highest Mg content shows the highest Hall mobility of ~930 cm^2/Vs at 65 K [112].

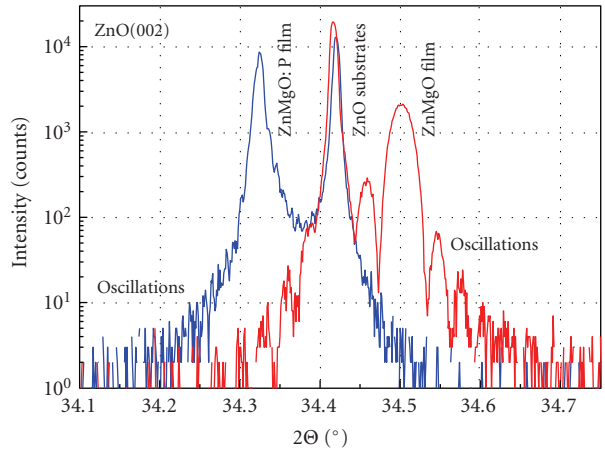

Figure 29: ZnO(002) HR-XRD triple axis $2\Theta - \omega$ scans of a homoepitaxial $Zn_{0.965}Mg_{0.025}P_{0.01}O$ film E1917 (blue) and a $Zn_{0.96}Mg_{0.04}O$ QW film E2000 (red) which exhibit compressive and tensile in-plane strain in the pseudomorphic growth mode, respectively. The total film thickness (calculated from the intensity oscillations) and the out-of-plane strain were 1,030 nm and 330 nm and 0.27% and −0.22% for E1917 (blue) and E2000 (red), respectively.

6. Oxide Multilayers with Smooth Interfaces

The interface smoothness of ZnO quantum wells (QWs) with MgZnO barriers could be considerably improved so that the QW photoluminescence gives evidence of the quantum-confined Stark effect, which was up to now observed only in MBE and MOCVD grown ZnO QWs (Section 6.1). By in-situ RHEED control, we are able to grow monolayer controlled $SrTiO_3/BaTiO_3$ single and multilayers with atomically flat interfaces and surfaces (Section 6.2.).

6.1. Improved Interface Abruptness of MgZnO/ZnO Quantum Wells Grown by PLD. Due to the polar nature of ZnO and MgZnO, both materials possess a spontaneous polarization parallel to their crystallographic c-axis. The magnitude depends on the Mg content, and a sheet charge forms in MgZnO/ZnO heterostructures if the heterointerface intersects the c-axis. An electric field arises from the interface charge in MgZnO quantum wells. Holes and electrons will be separated leading to the quantum-confined Stark effect

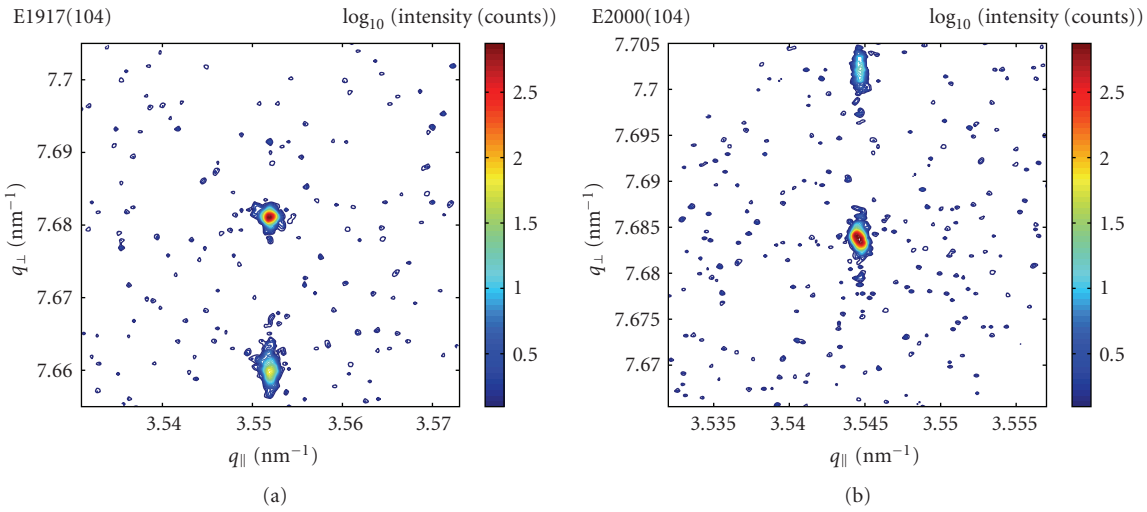

FIGURE 30: HR-XRD triple-axis reciprocal space maps (RSMs) of the asymmetric (104) reciprocal lattice points of films and substrates of the two homoepitaxial samples E1917 and E 2000 (compare Figure 29). In the center of the maps is the ZnO (104) substrate lattice point with higher intensity, and below or above is the weaker ZnMgO:P and ZnMgO (104) film lattice point. The perfect vertical alignment of (104) film and substrate peaks demonstrates the in-plane lattice match and the pseudomorphic growth mode.

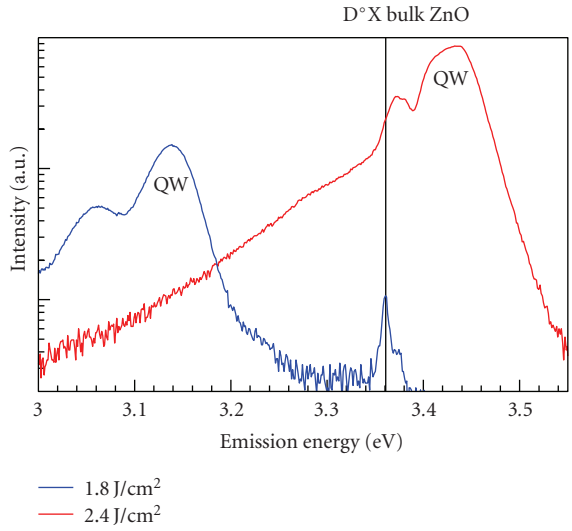

FIGURE 31: PL-spectra of MgZnO/ZnO QW grown by PLD at high fluence (2.4 J/cm^2, red line) and low fluence (1.8 J/cm^2, blue line). The donor bound excitonic emission (D^0X) of bulk ZnO is indicated by a black line, and the QW emission is marked in the spectra. The quantum well grown at low laser fluence shows the quantum confined Stark effect due to improved interface sharpness, while the other does not.

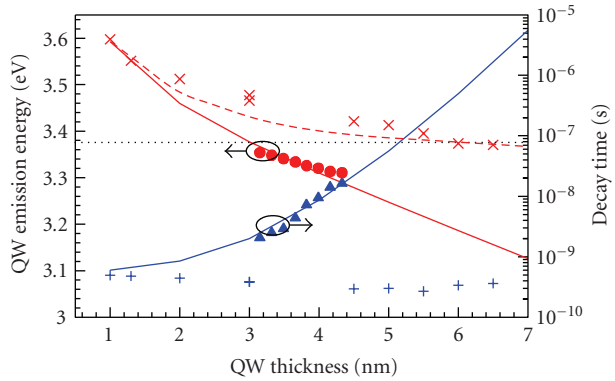

FIGURE 32: Dependence of the photoluminescence energy (left scale) and decay time (right scale) taken at the maximum of the QW luminescence of PLD grown QW samples (Figure 31), on the thickness of the ZnO quantum wells. Closed symbols give data obtained in [76] with remarkable QCSE. Crosses symbolize data from PLD grown samples without remarkable QCSE [77]. The black dotted line shows the free exciton transition energy in bulk ZnO. Solid lines give the expected dependence from the variational calculations with the presence of an electrical polarization mismatch. The dashed red line gives the transition energy as from variational calculations without a mismatch in the electrical polarization.

(QCSE). An abrupt interface is required for the occurrence of the QCSE.

Quantum confinement effects in $Mg_xZn_{1-x}O$/ZnO quantum wells (QWs) grown by PLD were previously published [77]. We were able to control the thickness of the QWs in the range from 4.8 nm down to 1.2 nm, and the energetic position of the QW emission shifted accordingly. However, even for high QW widths no significant influence of the QCSE on the 2 K photoluminescence was detected [77].

In recent experiments, the laser fluence in the PLD process was controlled in order to modify the energy of the particles in the laser plasma. This had a tremendous influence on the sharpness of the heterointerfaces. For a reduced laser fluence of 1.8 J/cm^2, a systematic redshift of the QW luminescence with increasing well width of up to 230 meV (Figure 31) below the emission of the free exciton in bulk ZnO was observed [76]. For samples grown at a high fluence (2.4 J/cm^2), the luminescence peak barely shifts

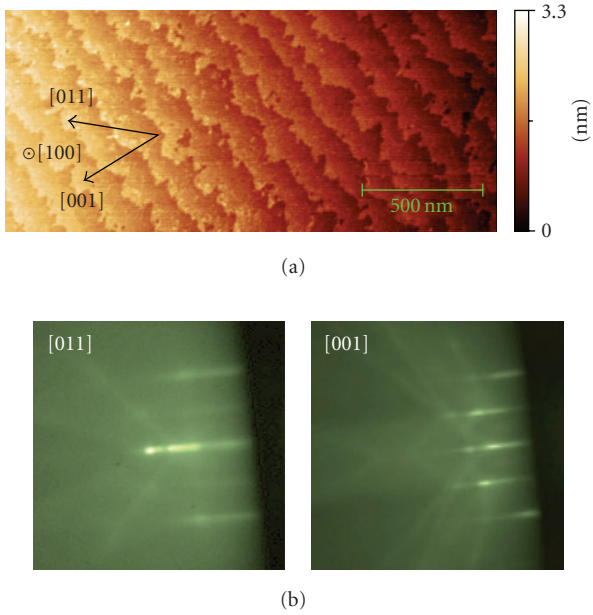

Figure 33: Atomic Force Microscopy (AFM) image of a typical STO(100) substrate surface after etching and heat treatment, with unit cell steps of 3.9 Å height. Below are the corresponding RHEED surface images taken in [011] and [001] directions.

below the emission of bulk ZnO, indicating the absence of a strong electric field in the quantum well, as mentioned above. Additionally, an increase in the exciton lifetime by two orders of magnitude with increasing thickness is observed for the samples grown with the low fluence, while no change is observed for the samples grown with the high fluence, as shown in Figure 32.

These results were explained by a difference in the kinetic energies of the constituents of the laser plasma. For a high laser fluence, the ions in the plasma have sufficient energy to penetrate the topmost layers of the growing film, resulting in an intermixing between the ZnO QW and the MgZnO barrier, which leads to a reduction of the electric field in the QW [76]. A similar diminishing of the QCSE was seen after ion bombardement of MBE grown MgZnO/ZnO QWs that previously showed the QCSE [113].

6.2. PLD of $SrTiO_3$ and $BaTiO_3$ Multilayers with In Situ RHEED. We report the growth of $SrTiO_3$ (STO) and $BaTiO_3$ (BTO) thin films using PLD combined with high-pressure Reflection High Energy Electron Diffraction (RHEED) system (STAIB "Torr RHEED" with double differentially pumped 35 keV gun) to control the growth rate as well as the surface quality of the thin films with submonolayer resolution. References [114–119] describe the state of the art of the so-called laser MBE technique which is a common name for PLD with in-situ RHEED.

The thin films were grown on STO (100) substrates supplied from Crystal GmbH Berlin. A thermal annealing step has been applied in order to obtain a TiO_2-terminated, monolayer surface quality of the substrates, as shown in Figure 33. The substrates were pretreated for 30 seconds with NH_4F-HF solution and subsequently annealed for 2 hours at 870°C in 700 mbar oxygen ambient.

For the growth of the thin films, the substrate temperature T_{sub}, the oxygen partial pressure $p(O_2)$ and the laser fluence at the target F are varied between 580°C and 720°C, 0.01 mbar and 0.0003 mbar, and between 1.6 J/cm^2 and 2.5 J/cm^2, respectively. During the PLD process, RHEED monitors the film growth on line by high speed recording a continuous movie file with up to 50 RHEED patterns per second which reflect the changes of surface morphology. This technique is very surface sensitive and enables to study, for example, whether a two-dimensional layer by layer (or step-flow) growth or a three-dimensional island growth dominates under the chosen PLD parameters; see for comparison [117, 118]. By growing STO homoepitaxially on pretreated STO substrates, we are able to observe intensity oscillations of the specular RHEED (0,0) spot indicating a layer by layer growth. The characteristic of the RHEED spot intensity as a function of time for the STO film growth is shown in Figure 34(a). The oscillations are visible over the whole recording time interval of 400 sec. and even remain intense and clearly resolved when the repetition rate of the laser is changed from 1 Hz to 3 Hz. The RHEED images recorded at the marked time positions show streaky lines supporting the conclusion of a layer by layer growth. As to the pulsed nature of PLD, the RHEED oscillations show a substructure related to the time regime of the single laser pulses, as shown in Figure 34(b).

By looking on the AFM image of the STO film surface after 3000 laser pulses, obviously monoatomic steps as predetermined by the substrate are still visible; see Figure 35.

By growing BTO on STO(100), RHEED oscillations are still visible. We observe that in the case of a too small laser flux the BTO growth mode changes from layer by layer growth to a three dimensional island growth as shown in Figure 36. The spotty RHEED images clearly indicate the formation of 3-dimensional BTO islands. After finding optimal BTO growth parameters, we were able to preserve the layer by layer growth regime also for BTO, which enables us to grow heterostructures of alternating STO and BTO thin film multilayers. As shown in Figure 37, the RHEED-oscillations remain visible even after growing two double layers of STO and BTO, thus enabling the growth of high quality STO/BTO superlattices.

7. Summary

Recent experimental progress of several advanced PLD techniques for growth of oxide films and multilayers is reported. Large-area PLD is demonstrated for double-sided $CeO_2/YBa_2Cu_3O_{7-\delta}$ films on both sides of r-plane sapphire wafers of 71 × 75 mm^2 size, corresponding to a diagonal of 4-inch, for microwave filter applications, and for thin ZnMgO films on 50 × 50 mm^2 a-plane sapphire substrates for field effect transistor demonstrators. Large-area Bragg reflectors built from 10 pairs Al_2O_2/YSZ with

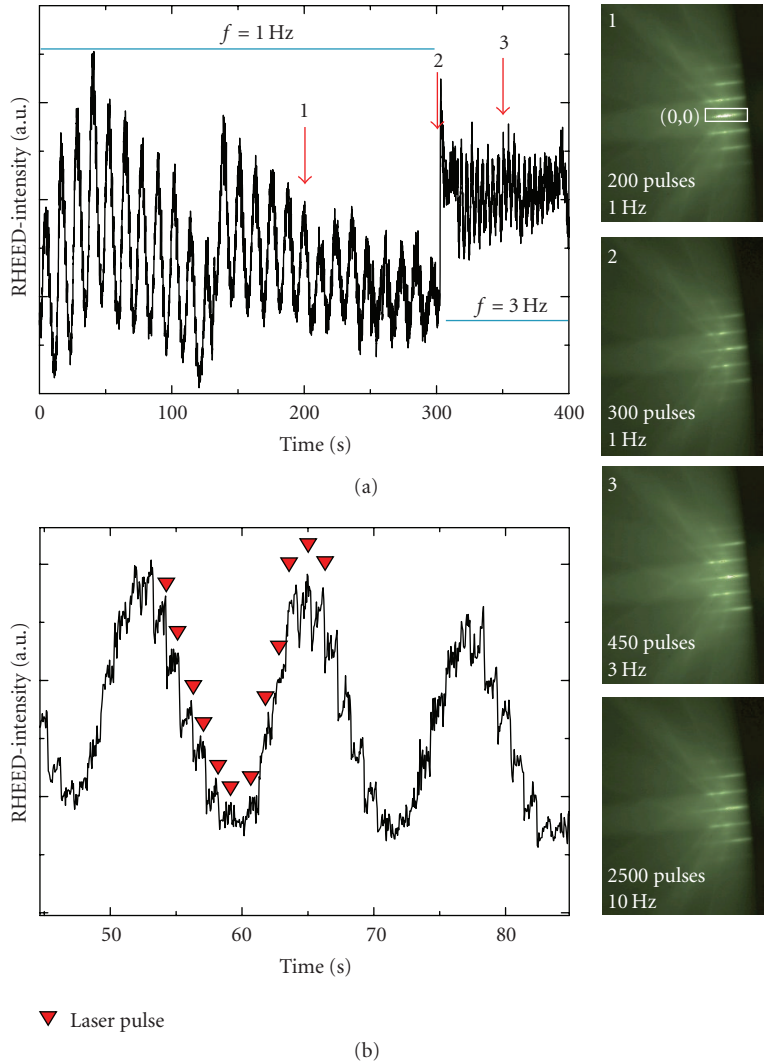

FIGURE 34: (a) RHEED oscillations during the growth of an STO thin film at $T_{sub} \approx 700°C$, $p(O_2) = 0.002$ mbar, and $F \approx 1.9$ J/cm^2. The oscillations are visible over the whole measurement time even for a laser repetition frequency of 3 Hz. The time positions 1, 2, 3 correspond to the recording of the RHEED images marked 1, 2, 3 (right). In RHEED image no. 1, the specular (0,0) spot is framed which is used for recording the oscillations throughout this section. (b) A detailed look on three RHEED oscillations during growth with 1 Hz. A substructure related to the single laser pulses (marked by red triangles) is resolved. One STO monolayer is grown with 12 pulses.

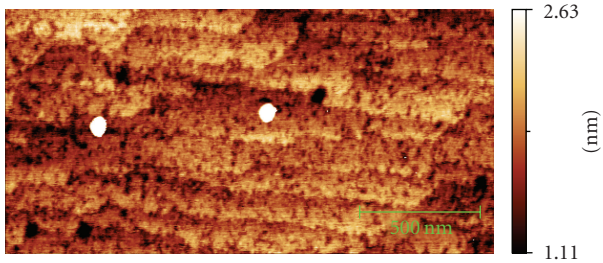

FIGURE 35: AFM image of an STO thin film at $T_{sub} \approx 700°C$, $p(O_2) = 0.002$ mbar, and $F \approx 1.9$ J/cm^2 on a pre- treated STO (100) substrate. The thickness of the STO thin film is about 95 nm.

total thickness around 1 μm show high optical homogeneity within 40 mm diameter. The unique flexibility of PLD concerning the deposited material was utilized for extended doping and alloying of ZnO thin films for future optoelectronic applications, and for doped $BaTiO_3$ thin films with optimized dielectric properties within a certain temperature range. The amount of trace impurities in the PLD grown films is discussed, and process-related sources of impurities as the ball mills for PLD target preparation were considered in detail. By the introduction of low-temperature interlayers, the dislocation density in heteroepitaxial ZnO thin films on c-sapphire was reduced to achieve high Hall mobilities above 150 cm^2/Vs at 300 K. ZnO homoepitaxy on single crystalline ZnO substrates is a further possibility to grow films with very low dislocation density and corresponding high Hall mobilities of more than 900 cm^2/Vs at 65 K. The interface abruptness of PLD grown ZnO quantum wells with MgZnO barriers could be considerably

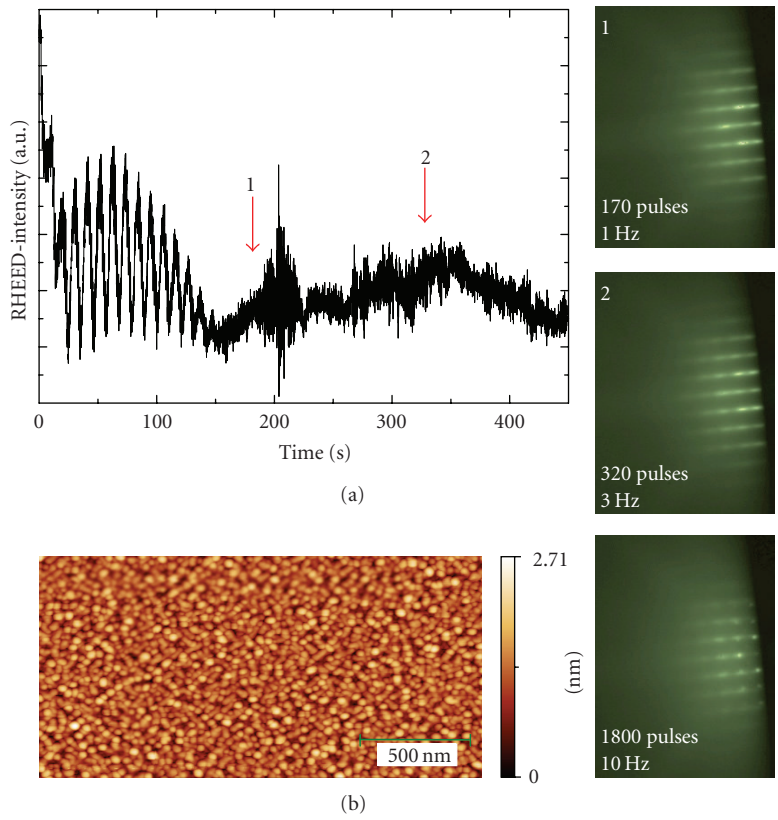

Figure 36: (a) RHEED intensity as function of time for a BTO thin film grown at $T_{sub} \approx 700^{\circ}C$, $p(O_2) = 0.002$ mbar, and $F \approx 1.9\,J/cm^2$. Still in the 1 Hz regime, the growth mode changes from layer by layer growth with clear oscillations up to 150 sec., to an island growth from 150 to 450 sec. as indicated by the more and more spotty RHEED images (right). (b) AFM image of the sample after 3,000 pulses. Clearly the granular surface with BTO islands is visible as implied by the RHEED images (right).

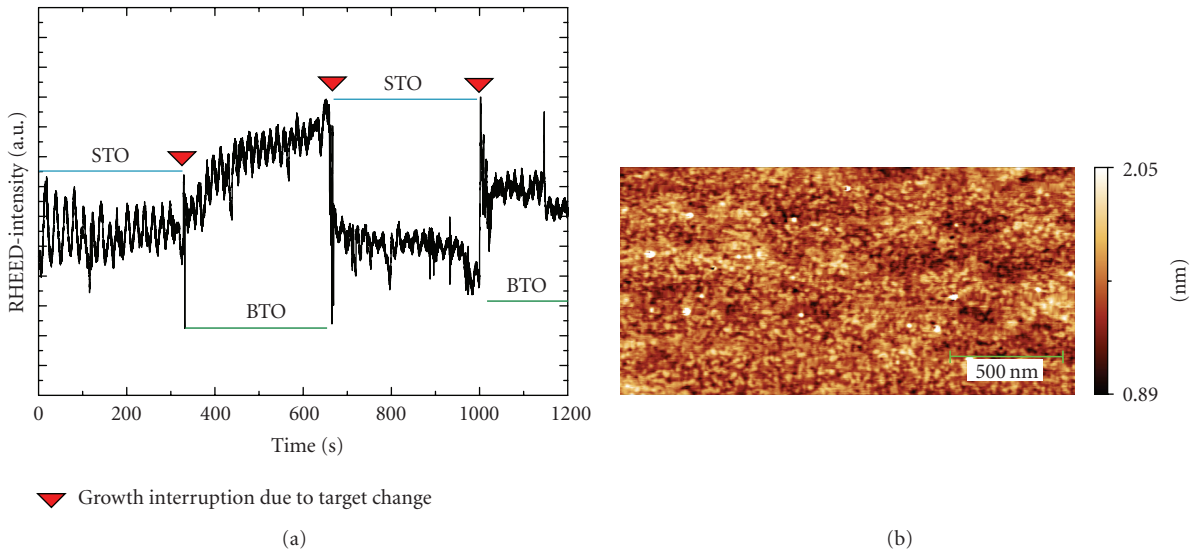

Figure 37: (a) RHEED (0,0) spot intensity as function of time for a BTO/STO heterostructure grown at $T_{sub} \approx 700^{\circ}C$, $p(O_2) = 0.002$ mbar and $F \approx 2{,}5\,J/cm^2$ on STO(100). The oscillations are visible over the whole deposition time. The first STO layer is 16, and the following BTO layer is 21 monolayers thick. (b) AFM image after growth of two double layers of STO and BTO.

improved so that the optical QW emission gives evidence of the quantum-confined Stark effect. By in-situ RHEED control, we are able to grow monolayer controlled $SrTiO_3$/$BaTiO_3$ single- and multilayers with atomically flat interfaces and surfaces.

Acknowledgments

M. Lorenz and all coauthors thank D. Natusch and G. Ramm for their outstanding long-term engagement in development of the modular PLD growth systems and for SNMS depth profiling and PLD target preparation, respectively. They thank R. Heidinger, Karlsruhe Research Center for the microwave characterization of the BTO films within the industrial integrated BMBF Project FKZ 13N8158. G. Wagner (Leipzig) and W. Mader (Bonn) prepared TEM cross sections of ZnO films on ZnO and sapphire, respectively. Florian Schmidt was involved in the CV and TAS investigations of the ZnMgO films from targets prepared with different ball mills. J. Sellmann and S. Schöche optimized the growth of the Bragg reflectors and the STO substrate pretreatment, respectively. M. Thorwart worked at the PLD with in-situ RHEED monitoring. Current financial support of the Deutsche Forschungsgemeinschaft within the SFB 762 "Functionality of oxide interfaces," of the European Social Fund (ESF), and the Leipzig School of Natural Sciences BuildMoNa (GS 185) is gratefully acknowledged.

References

[1] D. B. Chrisey and G. H. Hubler, Eds., *Pulsed Laser Deposition of Thin Films*, Wiley, New York, NY, USA, 1994.

[2] R. Eason, Ed., *Pulsed Laser Deposition of Thin Films—Applications-Led Growth of Functional Materials*, Wiley-Interscience, Hoboken, NJ, USA, 2007.

[3] D. Dijkkamp, T. Venkatesan, X. D. Wu et al., "Preparation of Y-Ba-Cu oxide superconductor thin films using pulsed laser evaporation from high Tc bulk material," *Applied Physics Letters*, vol. 51, no. 8, pp. 619–621, 1987.

[4] B. Roas, L. Schultz, and G. Endres, "Epitaxial growth of $YBa_2Cu_3O_{7-x}$ thin films by a laser evaporation process," *Applied Physics Letters*, vol. 53, no. 16, pp. 1557–1559, 1988.

[5] D. Bäuerle, "Laser chemical processing," in *Landolt-Börnstein New Series, Group VIII Advanced Materials and Technologies, Vol. 1 Laser Physics and Applications, Subvolume C Laser Applications*, R. Poprawe, H. Weber, and G. Herziger, Eds., pp. 311–354, Springer, Berlin, Germany, 2004.

[6] M. Lorenz, "Pulsed laser deposition of ZnO-based thin films," in *Transparent Conductive Zinc Oxide. Basics and Applications in Thin Film Solar Cells*, K. Ellmer, A. Klein, and B. Rech, Eds., vol. 104, chapter 7, pp. 303–358, Springer Series in Materials Science, Berlin, Germany, 2008.

[7] S. B. Ogale, Ed., *Thin Films and Heterostructures for Oxide Electronics*, Multifunctional Thin Films Series, edited by O. Auciello and R. Ramesh, Springer Science + Business Media, New York, NY, USA, 2005.

[8] C. Jagadish and S. Pearton, Eds., *Zinc Oxide Bulk, Thin Films and Nanostructures: Processing, Properties and Applications*, Elsevier, Amsterdam, The Netherlands, 2006.

[9] M. Lorenz, H. Hochmuth, D. Natusch et al., "Ag-doped double-sided PLD-YBCO thin films for passive microwave devices in future communication systems," *IEEE Transactions on Applied Superconductivity*, vol. 9, no. 2, pp. 1936–1939, 1999.

[10] M. Lorenz, H. Hochmuth, D. Natusch et al., "High-quality Y-Ba-Cu-O thin films by PLD—ready for market applications," *IEEE Transactions on Applied Superconductivity*, vol. 11, no. 1, pp. 3209–3212, 2001.

[11] M. Lorenz, H. Hochmuth, D. Natusch, and M. Grundmann, "High-quality reproducible PLD Y-Ba-Cu-O:Ag thin films up to 4 inch diameter for microwave applications," *Physica C*, vol. 372–376, no. 2, pp. 587–589, 2002.

[12] C. Curran, *Gepulste Laserabscheidung von Aurivillius-Phasen für ferroelektrische dunne Schichten*, Ph.D. thesis, Martin-Luther-Universität Halle-Wittenberg, 1997.

[13] R. Klarmann, *Laserdeposition ferroelektrischer $(Pb_{0.92}La_{0.08})(Zr_{0.65}Ti_{0.35})O_3$-Schichten auf Edelstahlsubstraten*, Ph.D. thesis, Universität Augsburg (Shaker, Aachen), 2000.

[14] G. Köbernik, *Präparation und Charakterisierung ferroelektrischer perowskitischer Multilagen*, Ph.D. thesis, Technische Universität Dresden, 2004.

[15] M. Maier, *In-situ Präparation von komplexen supraleitenden und ferroelektrischen Heterostrukturen mittels gepulster Laser Deposition*, Ph.D. thesis, Universität Mainz, 2001.

[16] M. Mertin, *Modellierung des PLD-Prozesses zur Abscheidung elektrokeramischer Dünnschichten*, Ph.D. thesis, D82 RWTH Aachen (Shaker Aachen), 1996.

[17] A. I. Petraru, *Optical and electro-optical properties of $BaTiO_3$ thin films and Mach-Zehnder waveguide modulators*, Ph.D. thesis, Universität Köln, 2003.

[18] M. Siegert, *Wachstumsuntersuchungen an Bariumtitanat-Dünnschichten, hergestellt mit gepulster Laserdeposition*, Ph.D. thesis, Universität Köln, 2001.

[19] S. Bar, *Crystalline, rare-earth-doped sesquioxide PLD-films on α-alumina*, Ph.D. thesis, Universität Hamburg, Göttingen, Germany, 2004.

[20] J. Goldfuß, *Herstellung und Modifizierung heteroepitaktischer Oxidschichten auf Si*, Ph.D. thesis, Universität Augsburg (Verlag für Wissenschaft und Forschung), Berlin, Geramny, 2005.

[21] B. Hobein, *Herstellung von dünnen Elektrolytschichten mittels Laserablation und Kathodenzerstaubüng für Hochtemperatur-Brennstoffzellen*, Ph.D. thesis, RWTH Aachen, 2003.

[22] R. Hühne, *Textur- und Mikrostrukturentwicklung bei der ionenstrahlunterstutzten Laserdeposition von MgO*, Ph.D. thesis, Technische Universität Dresden, 2001.

[23] B. Keiper, *Ionengestützte Laserpulsabscheidung von Oxidschichten für optische Anwendungen*, Ph.D. thesis, Technische Universität Chemnitz, 1997.

[24] Y. Kuzminykh, *Crystalline, Rare-Earth-doped Sesquioxide and YAG PLD -Films*, Ph.D. thesis, Universität Hamburg, 2006.

[25] L. Ferchland, *Untersuchungen zum Wachstum und zur Passivierung von dünnen Schichten aus Hochtemperatur-Supraleitern für die Anwendung bei Sensorbauelementen*, Ph.D. thesis, Fortschritt-Berichte VDI-Reihe 9 Elektronik/Mikro- und Nanotechnik, Nr. 320 (VDI-Verlag Düsseldorf), 2000.

[26] B. Schey, *Laserdeposition großflachiger $YBa_2Cu_3O_{7-x}$-Schichten auf einkristallinen und technischen Substraten mit Textur-Untersuchungen zur ionenunterstutzten Laserablation von Ceroxid*, Ph.D. thesis, Universität Augsburg (Shaker, Aachen), 1998.

[27] B. Worz, *Wachstum biaxial texturierter NiO-Schichten auf chemisch behandelten Ni-5%W-RABiTS und gepulste*

Laserdeposition epitaktischer Schichten für die Herstellung supraleitender $YBa_2Cu_3O_{7-\delta}$—Bänder, Ph.D. thesis, Universität Augsburg (Mensch & Buch Verlag Berlin 2004), 2003.

[28] J. Hohage, *Synthese von Bornitridschichten mittels PLD-Verfahren*, Ph.D. thesis, Technische Universität Dresden, 2004.

[29] S. Six, *Synthese epitaktischer Aluminiumoxidschichten mittels ionenstrahlgestützter Laserablation*, Ph.D. thesis, Universität Augsburg (Mensch & Buch Verlag Berlin), 2001.

[30] A. Gorbunoff, *Laser-Assisted Synthesis of Nanostructured Materials*, Habilitation thesis, TU Dresden, Fortschritt-Berichte VDI-Reihe 9 Elektronik/Mikro- und Nanotechnik, Nr. 357 (VDI-Verlag Düsseldorf), 2002.

[31] L. Roussak, *Herstellung und Charakterisierung von epitaktischen 2($ZnD_x(CuInD_2)_{1-x}$—Hetero- und Doppelheteroschichtstrukturen für D = S, Se und Te mittels Pulsed Laser Deposition (PLD)*, Ph.D. thesis, Universität Leipzig, 2005.

[32] S. Braun, *Gefüge- und Grenzflächenbeschaffenheit von Mo/Si-Multischichten, synthetisiert mittels Puls-Laser- und Magnetron-Sputter-Deposition*, Ph.D. thesis, Universität Bielefeld, 2004.

[33] U. Hannemann, *Wachstum, Mikrostruktur und hartmagnetische Eigenschaften von Nd-Fe-B-Schichten*, Dissertation, Technische Universität Dresden, 2004.

[34] T. Thärigen, *Makroskopische Eigenschaften und Mikrostruktur von Kohlenstoff-Dünnfilmen aus Laser-Plasma- Reaktionen von Graphit mit Stickstoff-Radikalen, Siliciumnitrid oder Bornitrid*, Ph.D. thesis, Universität Leipzig, 2000.

[35] Y. A. P. Mercado, *Diamond-like carbon and ceramic materials as protective coatings grown by pulsed laser deposition*, Ph.D. thesis, RWTH Aachen, 2003.

[36] A. Sewing, *Präparation von Ni-C-Multischichten und Mischsystemen mit dem PLD-Zweistrahlverfahren und Untersuchung der thermischen Stabilität der Schichtsysteme*, Ph.D. thesis, Technische Universität Dresden, 2002.

[37] C. Jin, *Growth and Characterization of ZnO- and ZnO-based alloys $Mg_xZn_{1-x}O$ and $Mn_xZn_{1-x}O$*, Ph.D. thesis, North Carolina State University, Raleigh, 2003.

[38] T. Nobis, *Beobachtung und Modellierung des optischen Flustergallerie-Effekts in hexagonalen Zinkoxid- Nanoresonatoren*, Ph.D. thesis, Universität Leipzig, 2006.

[39] A. Rahm, *Pulsed laser deposition growth and characterization of ZnO-based nanostructures*, Ph.D. thesis, Universität Leipzig, 2007.

[40] C. Czekalla, *Ortsaufgelöste Lumineszenz von Zinkoxid-Mikronadeln*, Ph.D. thesis, Universität Leipzig, 2009.

[41] M. Brandt, *Influence of the electric polarization on carrier transport and recombination dynamics in ZnO-based heterostructures,*, Ph.D. thesis, Universität Leipzig, 2010.

[42] M. S. Tillack, D. Blair, and S. S. Harilal, "The effect of ionization on cluster formation in laser ablation plumes," Report UCSD-ENG-103, University of California, San Diego, Calif, USA, August 2003.

[43] M. Lorenz, *Gepulste Laser-Plasmaabscheidung (PLD) von oxidischen Dünnfilm- und Heterostrukturen*, Habilitation thesis, Universität Leipzig, 2008.

[44] M. Lorenz, E. M. Kaidashev, H. von Wenckstern et al., "Optical and electrical properties of epitaxial $(Mg, Cd)_xZn_{1-x}O$, ZnO, and ZnO:(Ga,Al) thin films on c-plane sapphire grown by pulsed laser deposition," *Solid-State Electronics*, vol. 47, no. 12, pp. 2205–2209, 2003.

[45] J. Narayan and B. C. Larson, "Domain epitaxy: a unified paradigm for thin film growth," *Journal of Applied Physics*, vol. 93, no. 1, pp. 278–285, 2003.

[46] M. Lorenz, H. Hochmuth, and D. Natusch, "Waferheizer für Saphirsubstrate, Deutsche Patentanmeldung," Az. DE 102 55 453.7 vom 28.11.2002 (über Robert BOSCH GmbH Stuttgart).

[47] S. Ohashi, M. Lippmaa, N. Nakagawa, H. Nagasawa, H. Koinuma, and M. Kawasaki, "Compact laser molecular beam epitaxy system using laser heating of substrate for oxide film growth," *Review of Scientific Instruments*, vol. 70, p. 178, 1999.

[48] M. Lorenz, A. Rahm, B. Cao et al., "Self-organized growth of ZnO-based nano-and microstructures," *Physica Status Solidi B*, vol. 247, no. 6, pp. 1265–1281, 2010.

[49] C. Grüner, *Untersuchung des PLD-Laserplasmas mittels Optischer Emissionsspektroskopie*, M.S. thesis, University Leipzig, Institute for Experimental Physics II, 2009.

[50] M. Benamara, Z. Liliental-Weber, J. H. Mazur et al., "The role of the multi buffer layer technique on the structural quality of GaN," *MRS Internet Journal of Nitride Semiconductor Research*, vol. 5S1, W5.8, 2000.

[51] Y. Ralchenko, A. E. Kramida, J. Render, and the NIST ASD Team, "NIST Atomic Spectra Database version 3.1.5.," National Institute of Standards and Technology, Gaithersburg, Md, USA, September 2009, http://physics.nist.gov/asd3.

[52] J. E. Sansonetti and W. C. Martin, *Handbook of Basic Atomic Spectroscopic Data*, 2000.

[53] D. R. Lide, *Handbook of Chemistry and Physics*, CRC Press, Boca Raton, Fla, USA, 73rd edition, 1993.

[54] M. Lorenz, M. Brandt, G. Wagner et al., "MgZnO:P homoepitaxy by pulsed laser deposition: pseudomorphic layer-by-layer growth and high electron mobility," in *Zinc Oxide Materials and Devices IV*, vol. 7217 of *Proceedings of SPIE*, San Jose, Calif, USA, January 2009.

[55] M. Lorenz, H. Hochmuth, H. Börner, D. Natusch, and K. Kreher, "Large area pulsed laser deposition of YBCO thin films and buffer layers on 3-inch wafers," in *Materials Research Society Symposium Proceedings*, vol. 341 of *Epitaxial Oxide Thin Films and Heterostructures*, pp. 189–194, San Francisco, Calif, USA, April 1994.

[56] H. Hochmuth and M. Lorenz, "Inductive determination of the critical current density of superconducting thin films without lateral structuring," *Physica C*, vol. 220, no. 1-2, pp. 209–214, 1994.

[57] G. Kästner, D. Hesse, M. Lorenz, R. Scholz, N. D. Zakharov, and P. Kopperschmidt, "Microcracks observed in epitaxial thin films of $YBa_2Cu_3O_{7-\delta}$ and $GdBa_2Cu_3O_{7--\delta}$," *Physica Status Solidi A*, vol. 150, no. 1, pp. 381–394, 1995.

[58] H. Hochmuth and M. Lorenz, "Side-selective and non-destructive determination of the critical current density of double-sided superconducting thin films," *Physica C*, vol. 265, no. 3-4, pp. 335–340, 1996.

[59] M. Lorenz, H. Hochmuth, D. Natusch et al., "Large-area double-side pulsed laser deposition of $YBa_2Cu_3O_{7-x}$ thin films on 3-in. sapphire wafers," *Applied Physics Letters*, vol. 68, no. 23, pp. 3332–3334, 1996.

[60] M. Lorenz, H. Hochmuth, D. Natusch et al., "Large-area and double-sided pulsed laser deposition of Y-Ba-Cu-O thin films applied to HTSC microwave devices," *IEEE Transactions on Applied Superconductivity*, vol. 7, no. 2, pp. 1240–1243, 1997.

[61] M. Lorenz, H. Hochmuth, D. Natusch, and K. Kreher, "Highly reproducible large-area and double-sided pulsed laser deposition of HTSC YBCO:Ag thin films for microwave applications," *Applied Physics A*, vol. 69, no. 7, pp. S905–S911, 1999.

[62] M. Lorenz, H. Hochmuth, M. Grundmann, E. Gaganidze, and J. Halbritter, "Microwave properties of epitaxial large-area Ca-doped $YBa_2Cu_3O_{7-\delta}$ thin films on *r*-plane sapphire," *Solid-State Electronics*, vol. 47, no. 12, pp. 2183–2186, 2003.

[63] T. Kaiser, *Nichtlineare Hochfrequenzeigenschaften von Hochtemperatursupraleiter-Filmen*, Ph.D. thesis, Bergische Universität Gesamthochschule Wuppertal, 1998.

[64] R. Semerad, B. Utz, P. Berberich, W. Prusseit, and H. Kinder, "Coevaporation of YBaCuO films up to 9-inches diameter," in *Applied Superconductivity*, Inst. Phys. Conf. Ser. No. 148, p. 847, IOP, Bristol, UK, 1995.

[65] J. Geerk, A. Zaitsev, G. Linker et al., "A 3-chamber deposition system for the simultaneous double-sided coating of 5-inch wafers," *IEEE Transactions on Applied Superconductivity*, vol. 11, no. 1, pp. 3856–3858, 2001.

[66] Y. Lemaître, D. Mansart, B. Marcilhac, J. C. Mage, and J. Siejka, "Double-sided sputtering deposition of $YBa_2Cu_3O_{7-\delta}$ thin films on $2''$ $LaAlO_3$ wafers for microwave applications," *IEEE Transactions on Applied Superconductivity*, vol. 9, no. 2, pp. 2363–2366, 1999.

[67] D. W. Face, F. M. Pellicone, R. J. Small, L. Bao, M. S. Warrington, and C. Wilker, "$Tl_2Ba_2CaCu_2O_8$ and $YBa_2Cu_3O_7$ films on large area MgO and sapphire substrates for high power microwave and rf applications," *IEEE Transactions on Applied Superconductivity*, vol. 9, no. 2, pp. 2492–2495, 1999.

[68] M. Klauda, T. Kässer, and B. Mayer, "Superconductors and cryogenics for future communication systems," *IEEE Transactions on Microwave Theory and Techniques*, vol. 48, no. 7, pp. 1227–1239, 2000.

[69] T. Kässer, M. Viertel, R. Bölter, C. Neumann, and F. Schnell, "Superconductors and cryotechnology for space communications," *Physica C*, vol. 372–376, no. 1, pp. 489–492, 2002.

[70] R. Schwab, R. Heidinger, J. Geerk, F. Ratzel, M. Lorenz, and H. Hochmuth, "Surface impedance mapping at cryogenic temperatures of HTSC wafers at 145 GHz," in *Proceedings of the 23th International Conference on Infrared and Millimeter Waves*, Essex, UK, September 1998.

[71] R. Schwab, *Ortsaufgelöste Untersuchung des Oberflachen-widerstandes von epitaktischen $YBa_2Cu_3O_{7-x}$- Dünnschichten mit Millimeterwellen*, Dissertation, FZ Karlsruhe/Universität Karlsruhe, 1999.

[72] H. Frenzel, A. Lajn, H. von Wenckstern et al., "Recent progress on ZnO-based metal-semiconductor field-effect transistors and their application in transparent integrated circuits," *Advanced Materials*.

[73] H. Frenzel, A. Lajn, H. von Wenckstern, and M. Grundmann, "Ultrathin gate-contacts for metal-semiconductor field-effect transistor devices: an alternative approach in transparent electronics," *Journal of Applied Physics*, vol. 107, no. 11, Article ID 114515, 2010.

[74] B. K. Meyer, H. Alves, D. M. Hofmann et al., "Bound exciton and donor-acceptor pair recombinations in ZnO," *Physica Status Solidi B*, vol. 241, no. 2, pp. 231–260, 2004.

[75] H. von Wenckstern, S. Weinhold, G. Biehne et al., "Donor levels in ZnO," *Advances in Solid State Physics*, vol. 45, pp. 263–274, 2005.

[76] M. Brandt, M. Lange, M. Stölzel et al., "Control of interface abruptness of polar MgZnO/ZnO quantum wells grown by pulsed laser deposition," *Applied Physics Letters*, vol. 97, no. 5, Article ID 052101, 2010.

[77] S. Heitsch, G. Zimmermann, A. Müller et al., "Interface and luminescence properties of pulsed laser deposited $Mg_xZn_{1-x}O$/ZnO quantum wells with strong confinement," in *Materials Research Society Symposium Proceedings*, vol. 957, pp. 229–234, Boston, Mass, USA, November 2007.

[78] C. Sturm, H. Hilmer, R. Schmidt-Grund, and M. Grundmann, "Observation of strong exciton-photon coupling at temperatures up to 410 K," *New Journal of Physics*, vol. 11, Article ID 073044, 2009.

[79] H. Hilmer, C. Sturm, R. Schmidt-Grund, B. Rheinländer, and M. Grundmann, "Observation of strong light-matter coupling by spectroscopic ellipsometry," *Superlattices & Microstructures*, vol. 47, no. 1, pp. 19–23, 2010.

[80] R. Schmidt-Grund, H. Hilmer, A. Hinkel et al., "Two-dimensional confined photonic wire resonators—strong light-matter coupling," *Physica Status Solidi B*, vol. 247, no. 6, pp. 1351–1364, 2010.

[81] C. Bundesmann, N. Ashkenov, M. Schübert et al., "Raman scattering in ZnO thin films doped with Fe, Sb, Al, Ga, and Li," *Applied Physics Letters*, vol. 83, no. 10, pp. 1974–1976, 2003.

[82] Q. Xu, L. Hartmann, H. Schmidt et al., "Metal-insulator transition in Co-doped ZnO: magnetotransport properties," *Physical Review B*, vol. 73, no. 20, Article ID 205342, 2006.

[83] Q. Xu, L. Hartmann, H. Schmidt et al., "Magnetoresistance in pulsed laser deposited 3d transition metal doped ZnO films," *Thin Solid Films*, vol. 515, no. 4, pp. 2549–2554, 2006.

[84] H. Schmidt, M. Diaconu, H. Hochmuth et al., "Electrical and optical spectroscopy on ZnO:Co thin films," *Applied Physics A*, vol. 88, no. 1, pp. 157–160, 2007.

[85] M. Ungureanu, H. Schmidt, H. von Wenckstern et al., "A comparison between ZnO films doped with 3d and 4f magnetic ions," *Thin Solid Films*, vol. 515, no. 24, pp. 8761–8763, 2007.

[86] H. von Wenckstern, G. Benndorf, S. Heitsch et al., "Properties of phosphorus doped ZnO," *Applied Physics A*, vol. 88, no. 1, pp. 125–128, 2007.

[87] C. Bundesmann, A. Rahm, M. Lorenz, M. Grundmann, and M. Schübert, "Infrared optical properties of $Mg_xZn_{1-x}O$ thin films ($0 \le x \le 1$): long-wavelength optical phonons and dielectric constants," *Journal of Applied Physics*, vol. 99, no. 11, Article ID 113504, 2006.

[88] R. Schmidt-Grund, A. Carstens, B. Rheinländer et al., "Refractive indices and band-gap properties of rocksalt $Mg_xZn_{1-x}O$ ($0.68 \le x \le 1$)," *Journal of Applied Physics*, vol. 99, no. 12, Article ID 123701, 2006.

[89] S. Heitsch, G. Zimmermann, D. Fritsch et al., "Luminescence and surface properties of $Mg_xZn_{1-x}O$ thin films grown by pulsed laser deposition," *Journal of Applied Physics*, vol. 101, no. 8, Article ID 083521, 2007.

[90] Q. Xu, H. Schmidt, H. Hochmuth et al., "Room temperature ferromagnetism in Nd- and Mn-codoped ZnO films," *Journal of Physics D*, vol. 41, no. 10, Article ID 105012, 2008.

[91] H. von Wenckstern, H. Schmidt, M. Brandt et al., "Anionic and cationic substitution in ZnO," *Progress in Solid State Chemistry*, vol. 37, no. 2-3, pp. 153–172, 2009.

[92] M. Lange, C. P. Dietrich, C. Czekalla et al., "Luminescence properties of ZnO/$Zn_{1-x}Cd_xO$/ZnO double heterostructures," *Journal of Applied Physics*, vol. 107, no. 9, Article ID 093530, 8 pages, 2010.

[93] D. Spemann, E. M. Kaidashev, M. Lorenz, J. Vogt, and T. Butz, "Ion beam analysis of epitaxial $(Mg, Cd)_xZn_{1-x}O$ and ZnO:(Li, Al, Ga, Sb) thin films grown on *c*-plane sapphire," *Nuclear Instruments and Methods in Physics Research, Section B*, vol. 219-220, no. 1-4, pp. 891–896, 2004.

[94] M. Khalid, M. Ziese, A. Setzer et al., "Defect-induced magnetic order in pure ZnO films," *Physical Review B*, vol. 80, no. 3, Article ID 035331, 2009.

[95] R. Waser, Ed., *Nanoelectronics and Information Technology—Advanced Electronic Materials and Novel Devices*, Wiley-VCH, Weinheim, Germany, 2003.

[96] J. F. Scott, "Applications of modern ferroelectrics," *Science*, vol. 315, no. 5814, pp. 954–959, 2007.

[97] M. Lorenz, H. Hochmuth, M. Schallner, R. Heidinger, D. Spemann, and M. Grundmann, "Dielectric properties of Fe-doped $Ba_xSr_{1-x}TiO_3$ thin films on polycrystalline substrates at temperatures between -35 and +85°C," *Solid-State Electronics*, vol. 47, no. 12, pp. 2199–2203, 2003.

[98] L. C. Sengupta and S. Sengupta, "Electrical properties of doped BSTO-0.6 thin films," *Materials Research Innovations*, vol. 2, p. 278, 1999.

[99] S. S. Gevorgian and E. L. Kollberg, "Do we really need ferroelectrics in paraelectric phase only in electrically controlled microwave devices?" *IEEE Transactions on Microwave Theory and Techniques*, vol. 49, no. 11, pp. 2117–2124, 2001.

[100] R. R. Romanofsky et al., "616 element phased array antenna," in *Materials Research Society Symposium Proceedings*, vol. 720, H 4.1.1, 2002.

[101] K. J. Choi, M. Biegalski, Y. L. Li et al., "Enhancement of ferroelectricity in strained $BaTiO_3$ thin films," *Science*, vol. 306, no. 5698, pp. 1005–1009, 2004.

[102] E. M. Kaidashev, M. Lorenz, H. von Wenckstern et al., "High electron mobility of epitaxial ZnO thin films on c-plane sapphire grown by multistep pulsed-laser deposition," *Applied Physics Letters*, vol. 82, no. 22, pp. 3901–3903, 2003.

[103] H. von Wenckstern, H. Schmidt, C. Hanisch et al., "Homoepitaxy of ZnO by pulsed-laser deposition," *Physica Status Solidi*, vol. 1, no. 4, pp. 129–131, 2007.

[104] M. Lorenz, G. Wagner, A. Rahm et al., "Homoepitaxial ZnO thin films by PLD: structural properties," *Physica Status Solidi C*, vol. 5, no. 10, pp. 3280–3287, 2008.

[105] M. Brandt, H. von Wenckstern, H. Schmidt et al., "High electron mobility of phosphorous-doped homoepitaxial ZnO thin films grown by pulsed-laser deposition," *Journal of Applied Physics*, vol. 104, no. 1, Article ID 013708, 2008.

[106] H. von Wenckstern, M. Brandt, H. Schmidt et al., "Properties of homoepitaxial ZnO and ZnO:P thin films grown by pulsed-laser deposition," in *Zinc Oxide Materials and Devices III*, vol. 6895 of *Proceedings of SPIE*, San Jose, Calif, USA, January 2008.

[107] M. Brandt, H. von Wenckstern, C. Dietrich et al., "Dopant activation in homoepitaxial MgZnO:P thin films," *Journal of Vacuum Science & Technology B*, vol. 27, p. 1604, 2009.

[108] Y. W. Heo, S. J. Park, K. Ip, S. J. Pearton, and D. P. Norton, "Transport properties of phosphorus-doped ZnO thin films," *Applied Physics Letters*, vol. 83, no. 6, pp. 1128–1130, 2003.

[109] S. J. Pearton, D. P. Norton, K. Ip, Y. W. Heo, and T. Steiner, "Recent progress in processing and properties of ZnO," *Progress in Materials Science*, vol. 50, no. 3, pp. 293–340, 2005.

[110] H. von Wenckstern, G. Benndorf, S. Heitsch et al., "Properties of phosphorus doped ZnO," *Applied Physics A*, vol. 88, no. 1, pp. 125–128, 2007.

[111] M. Brandt, H. von Wenckstern, G. Benndorf, H. Hochmuth, M. Lorenz, and M. Grundmann, "Formation of a two-dimensional electron gas in ZnO/MgZnO single heterostructures and quantum wells," *Thin Solid Films*, vol. 518, no. 4, pp. 1048–1052, 2009.

[112] M. Lorenz, M. Brandt, M. Lange et al., "Homoepitaxial $Mg_xZn_{1-x}O$ ($0 \leq x \leq 0.22$) thin films grown by pulsed laser deposition," *Thin Solid Films*, vol. 518, no. 16, pp. 4623–4629, 2010.

[113] J. A. Davis and C. Jagadish, "Ultrafast spectroscopy of ZnO/ZnMgO quantum wells," *Laser and Photonics Reviews*, vol. 3, no. 1-2, pp. 85–96, 2009.

[114] T. M. Shaw, A. Gupta, M. Y. Chern, P. E. Batson, R. B. Laibowitz, and B. A. Scott, "Atomic scale oxide superlattices grown by RHEED controlled pulsed laser deposition," *Journal of Materials Research*, vol. 9, no. 10, pp. 2566–2573, 1994.

[115] T. Matsumoto, H. Tanaka, K. Kouguchi, T. Kawai, and S. Kawai, "A scanning tunneling microscopy study of laser molecular beam epitaxy on $SrTiO_3(100)$ surface," *Surface Science*, vol. 312, no. 1-2, pp. 21–30, 1994.

[116] D. H. A. Blank, G. J. H. M. Rijnders, G. Koster, and H. Rogalla, "In-situ monitoring during pulsed laser deposition using RHEED at high pressure," *Applied Surface Science*, vol. 127–129, pp. 633–638, 1998.

[117] G. Koster, *Artificially layered oxides by Pulsed Laser Deposition*, Ph.D. thesis, Universiteit Twente, Enschede, The Netherlands, 1999.

[118] J. Klein, *Epitaktische Heterostrukturen aus dotierten Manganaten*, Ph.D. thesis, Universität Köln, 2001.

[119] H. Y. Hwang, "Atomic control of the electronic structure at complex oxide heterointerfaces," *MRS Bulletin*, vol. 31, no. 1, pp. 28–35, 2006.